AGU PUBLICATIONS

JGR

Journal of Geophysical Research: Space Physics

RESEARCH ARTICLE
10.1002/2016JA022978

Key Points:
- Vertically propagating IGWs are retrieved from meteor radar winds observed at King Sejong Station, Antarctica
- Low-frequency IGWs with intrinsic frequencies of $|f| - 3|f|$ occur frequently near the southern mesopause throughout a whole year
- Horizontal propagation directions of the low-frequency IGWs arerelated to the tropospheric and stratospheric jet flow systems

Supporting Information:
- Supporting Information S1

Correspondence to:
I.-S. Song,
isong@kopri.re.kr

Citation:
Song, I.-S., C. Lee, J.-H. Kim, G. Jee, Y.-H. Kim, H.-J. Choi, H.-Y. Chun, and Y. H. Kim (2017), Meteor radar observations of vertically propagating low-frequency inertia-gravity waves near the southern polar mesopause region, *J. Geophys. Res. Space Physics*, *122*, doi:10.1002/2016JA022978.

Received 19 MAY 2016
Accepted 11 APR 2017
Accepted article online 18 APR 2017

Meteor radar observations of vertically propagating low-frequency inertia-gravity waves near the southern polar mesopause region

I.-S. Song[1], C. Lee[1], J.-H. Kim[1], G. Jee[1], Y.-H. Kim[2], H.-J. Choi[3], H.-Y. Chun[4], and Y. H. Kim[5]

[1]Division of Polar Climate Sciences, Korea Polar Research Institute, Incheon, South Korea, [2]Severe Storm Research Center, Ewha Womans University, Seoul, South Korea, [3]Korea Institute of Atmospheric Prediction Systems, Seoul, South Korea, [4]Department of Atmospheric Sciences, Yonsei University, Seoul, South Korea, [5]Department of Astronomy, Space Science and Geology, Chungnam National University, Daejeon, South Korea

Abstract Vertically propagating low-frequency inertia-gravity waves (IGWs) are retrieved from meteor radar winds observed at King Sejong Station (KSS: 62.22°S, 58.78°W), Antarctica. IGW horizontal winds extracted from temporal band-pass filtering in regular time-height bins show the frequent occurrence of IGWs with the downward phase progression and the counterclockwise rotation of their horizontal wind vectors with time (i.e., upward energy propagation) near the mesopause region throughout the whole year of 2014. The vertical wavelengths of the observed IGWs roughly range from 14 km to more than 20 km, which is consistent with previous observational studies on the mesospheric IGWs over Antarctica. Stokes parameters and rotary spectra computed from the hodographs of the IGW horizontal wind components reveal that the intrinsic frequencies of the upward propagating IGWs are $|f| - 3|f|$ with seasonal variations of the relative predominance between $|f| - 2|f|$ and $2|f| - 3|f|$, where f is the Coriolis parameter at KSS. The hodograph analysis also indicates that the N-S propagation is dominant in austral summer, while the NE-SW propagation is pronounced in austral winter. The propagation direction is discussed in relation to the generation of IGWs due to dynamical imbalances occurring in the tropospheric and stratospheric jet flow systems. Ray tracing results indicate that the N-S propagation in summer may be due to the jet flow systems roughly north of KSS and the NE-SW propagation in winter may be either the SW propagation from the jet flow systems northeast of KSS or the NE propagation (around the South Pole) from the south of Australia and Southern Indian and Pacific Oceans.

1. Introduction

Breaking of vertically propagating gravity waves (GWs) has been recognized as one of essential forcing mechanisms required to account for the observed global-scale flow in the mesosphere and lower thermosphere (MLT) region [*Lindzen*, 1981]. In fact, GWs play a crucial role in inducing seasonal cycles of zonal mean zonal flow, meridional circulations, and pole-to-pole meridional temperature gradients near the mesopause regions by driving observed wind off the radiative-equilibrium wind structure [see *Fritts and Alexander*, 2003; *Kim et al.*, 2003].

Breaking GWs also have impacts in the thermosphere and ionosphere. Seasonal variation of eddy diffusivity due to breaking GWs may be an important factor in accounting for the structure and variability of thermospheric constituents [*Qian et al.*, 2009]. Thermospheric variability in the high-latitude region can be associated with the breaking of GWs whose anisotropies vary depending on the evolution stages of stratospheric sudden warming [*Yiğit et al.*, 2013]. Secondary GWs due to breaking GWs can be additional sources of thermospheric and ionospheric perturbations [*Oyama and Watkins*, 2012; *Vadas and Liu*, 2013].

Optical observational studies on GWs in the mesopause region have been carried out using airglow images [*Taylor and Hapgood*, 1990; *Kim et al.*, 2004; *Nielsen et al.*, 2009; *Kim et al.*, 2010; *Suzuki et al.*, 2013a] and noctilucent cloud (NLC) images [*Fritts et al.*, 1993; *Chandran et al.*, 2009; *Pautet et al.*, 2011]. GWs shown in airglow and NLC images are often found to have horizontal wavelengths of less than 100 km and ground-based periods of less than 1 h. GW wind covariances (i.e., momentum fluxes) are crucial in estimating effects of interaction

between GWs and mean flow, and they have been studied using radar instruments such as medium-frequency (MF) Doppler radars [*Fritts and Vincent*, 1987; *Reid and Vincent*, 1987a; *Thorsen et al.*, 1997] and meteor radars [*Hocking*, 2005; *Fritts et al.*, 2010a; *Lee et al.*, 2013; *de Wit et al.*, 2014]. Similar to the cases of airglow images, GWs detected using MF radars are considered to have horizontal wavelengths of less than a couple of hundred kilometers and ground-based frequencies of less than 1 h [*Reid and Vincent*, 1987b].

Such small-scale and high-frequency GWs have received substantial attention in that they can induce large momentum fluxes, can propagate from the lower atmosphere to the mesopause region without severe dissipation or filtering, and thus can significantly affect the MLT dynamics [e.g., *Fritts and Vincent*, 1987; *Nastrom and Fritts*, 1992]. Yet these observational results should not lead to the conclusion that the effects of low-frequency inertia-gravity waves (IGWs) are minor in the light of GW mean flow interaction, since the airglow and NLC images may primarily capture GWs with relatively short horizontal wavelengths due to their limited field of view and thus may underestimate large-scale IGWs.

There have been some observational studies on IGWs in the mesopause region. These observations were mostly made in polar regions through incoherent scatter radar in Arctic areas [*Nicolls et al.*, 2010], lidar and MF radar [*Chen et al.*, 2013, 2016], and airglow images of long-lasting meteor trails [*Kim et al.*, 2004; *Suzuki et al.*, 2013b] in Antarctica. Observed IGWs are in common characterized by near-inertial intrinsic frequencies and large vertical wavelengths of more than 10 km. *Chen et al.* [2016] analyzed in a rigorous and quantitative way the spectral characteristics of persistent IGWs with periods of 3–10 h observed at McMurdo, Antarctica, using lidar temperature in June for a period of 5 years. The persistent 3–10 h IGWs were found to have vertical wavelengths of 20–30 km and to be certainly differentiated from the global-scale IGW modes (i.e., tidal waves), given that their vertical wavelengths are smaller than those of the high-frequency tidal waves [*Smith et al.*, 2004; *Du and Ward*, 2010]. It is interesting that *Nicolls et al.* [2010] and *Chen et al.* [2013] reported long-distance propagation (across the pole) of low-frequency IGWs that are spontaneously generated from the tropospheric and stratospheric jets. These reports suggest that persistent, relatively large-scale, and low-frequency IGWs may possibly be important in terms of the GW mean flow interaction in the polar mesopause region. Such potential importance of the horizontally long-range propagating IGWs implies that the GW mean flow interaction in the mesopause region may not be fully understood by considering the vertical GW propagation alone.

In the present study, we retrieve low-frequency IGWs, propagating slowly upward over large horizontal distances, near the southern polar mesopause region from meteor radar wind observed at King Sejong Station (KSS: 62.22°S, 58.78°W) throughout the whole year of 2014. Analysis of this yearlong wind data, not limited to a particular season, is expected to enable us to more fully understand characteristics of polar mesopause IGWs and their seasonal variations. The meteor radar in operation at KSS, basic characteristics of winds observed over KSS, and GW retrieval methods are described in section 2. The vertical propagation and frequent occurrence of IGWs in the southern polar mesopause region are reported, and the intrinsic frequencies and propagation characteristics are analyzed in section 3. Then, possible GW source mechanisms are discussed in section 4, based on the analysis of dynamical imbalances and ray tracing model results. Summary and conclusion are given in the last section.

2. Data and Analysis Methods

A VHF meteor radar has been in operation since March 2007 at KSS on the King George Island located about 150 km north of the Antarctic Peninsula. The radar system is composed of a cross-folded dipole transmitter and five receivers arranged to minimize mutual antenna coupling (see *Kim et al.* [2012] and *Lee et al.* [2013] for further details). Since 2012, the peak transmitter power has been increased from 8 kW to 12 kW, resulting in increase in the number of received echoes [*Jee et al.*, 2014]. In fact, in 2014, detected meteor radar echoes were about 17,500–35,000 per day, larger than 15,000–28,000 prior to the power upgrade. In the number of detected meteor radar echoes, the maximum occurred in January and the minimum in September.

Meteor echoes are observed within a radius of 250–300 km for the full range of zenith angles (Figures 1a and 1b). The detected echoes in a given period of time are locally clustered in space, and the clusters rotate counterclockwise around the center in a day in association with the Earth's rotation. That is, echo observation areas in a time period shorter than a day are smaller than the areas covered by the radius of 250–300 km. In January as well as September, the echo clusters are roughly found in the NW, SW, SE, and NE sectors within the observation radius at 00–06 UT, 06–12 UT, 12–18 UT, and 18–24 UT, respectively. In contrast to this subdaily

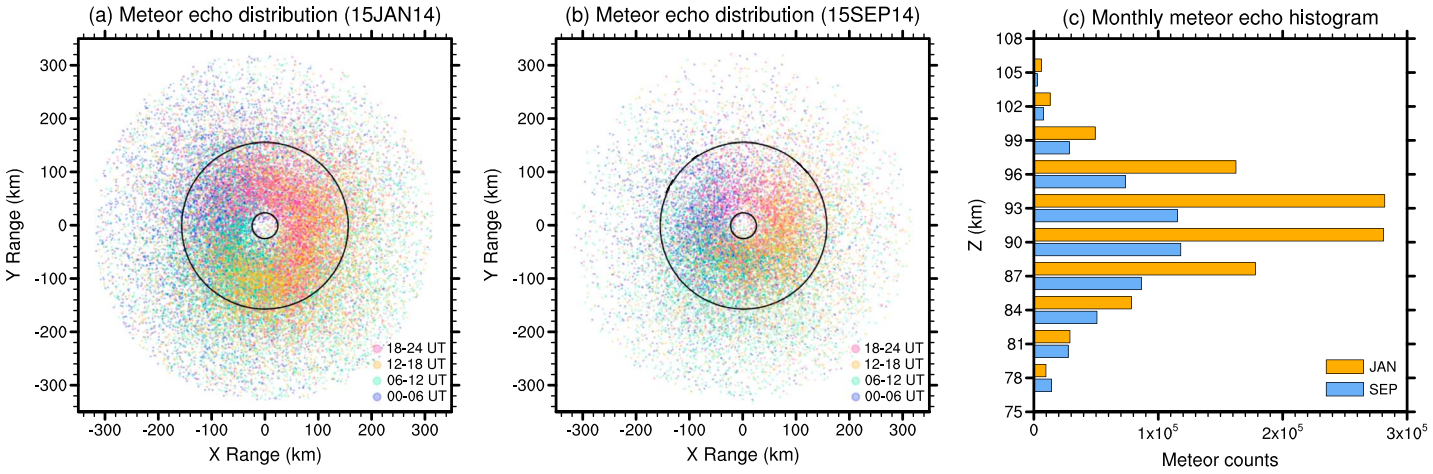

Figure 1. Horizontal and subdaily distributions of all meteor radar echoes observed in (a) 15 January 2014 and (b) 15 September 2014 and (c) the vertical histogram of the number of monthly meteor radar echoes for January and September. In Figures 1a and 1b, meteor echoes clustered in 00–06 UT, 06–12 UT, 12–18 UT, and 18–24 UT are plotted with 30% opacity in blue, green, orange, and red, respectively, and the inner and outer circles plotted in solid black denote the zenith angles of 15° and 60° for the height of 90 km, respectively. In Figure 1c, meteor echoes are binned in the regular 3 km height bins.

variation of echo locations, seasonal variation of echo locations is relatively small (not shown). In the vertical direction, radar echo detection is the most frequent at $z = 90 - 93$ km when echo heights are binned in the 3 km vertical grid (Figure 1c). The number of echoes below $z = 80$ km or above 100 km is only about $3 - 4\%$ ($8 - 9\%$) of maximum values at $z = 90 - 93$ km in January (September).

2.1. General Characteristics of Observed Large-Scale Winds

In order to understand basic characteristics of large-scale winds observed using a meteor radar at KSS, the three-dimensional wind components are determined using radial wind velocities observed from meteor echoes in the 1 h regular time bins and in eight height bins (80, 84.5, 88, 90.5, 92.5, 95, 98.5, and 103 km) with increasing height spacings (2, 3, 4, and 5 km) as being away from $z = 91.5$ km. In every time-height bin, the three wind components are computed in a least squares sense as in *Hocking and Thayaparan* [1997] for the zenith angles of 15°–60° only when the number of echoes is larger than 6 in each bin. Computed wind components are discarded as being unreliable (i.e., regarded as missing) when difference between the observed and computed radial velocities is larger than 25 m s^{-1}. The vertically varying height spacing is employed to obtain reliable wind data as much as possible in a deep atmospheric layer.

Figure 2 demonstrates vertically averaged power spectral densities (PSDs) of the hourly zonal and meridional wind components over KSS for the 1 year period. The computed wind components are unevenly sampled due to irregular distributions of missing values. Spectral analysis of these unevenly sampled data is achieved using the Lomb-Scargle (LS) periodogram method [*Lomb*, 1976; *Scargle*, 1982]. The LS periodogram method is equivalent to the least squares harmonic analysis (see *Scargle* [1982] for details) that has been used to extract tidal variations in previous observational studies [e.g., *Mitchell et al.*, 2002; *Lee et al.*, 2013; *de Wit et al.*, 2014]. In the computation of the LS periodograms, missing values are differently distributed in time depending on height bins, and thus, the LS periodograms are obtained at different frequency bins depending on heights. For this reason, the PSD at each height is interpolated in a regular reference frequency grid before vertical averaging.

The PSDs shown in Figure 2 indicate that the semidiurnal (12 h) tidal variation over KSS is the strongest among the variations associated with tides or planetary waves. The predominance of the 12 h tidal variation over KSS was also found in other observational results at geographical locations close to KSS [e.g., *Beldon and Mitchell*, 2010; *Fritts et al.*, 2010a] and modeling studies of tidal waves [*Smith*, 2012]. Besides the strong 12 h tidal variation, moderate diurnal (24 h) and weak terdiurnal (8 h) and quardiurnal (6 h) tidal variations and planetary wave oscillations with the periods of 2–24 days are also found. It seems reasonable from Figure 2 to state that these tidal waves and slowly varying planetary waves including constant mean winds characterize the large-scale flow in the mesopause region over KSS throughout the whole year of 2014.

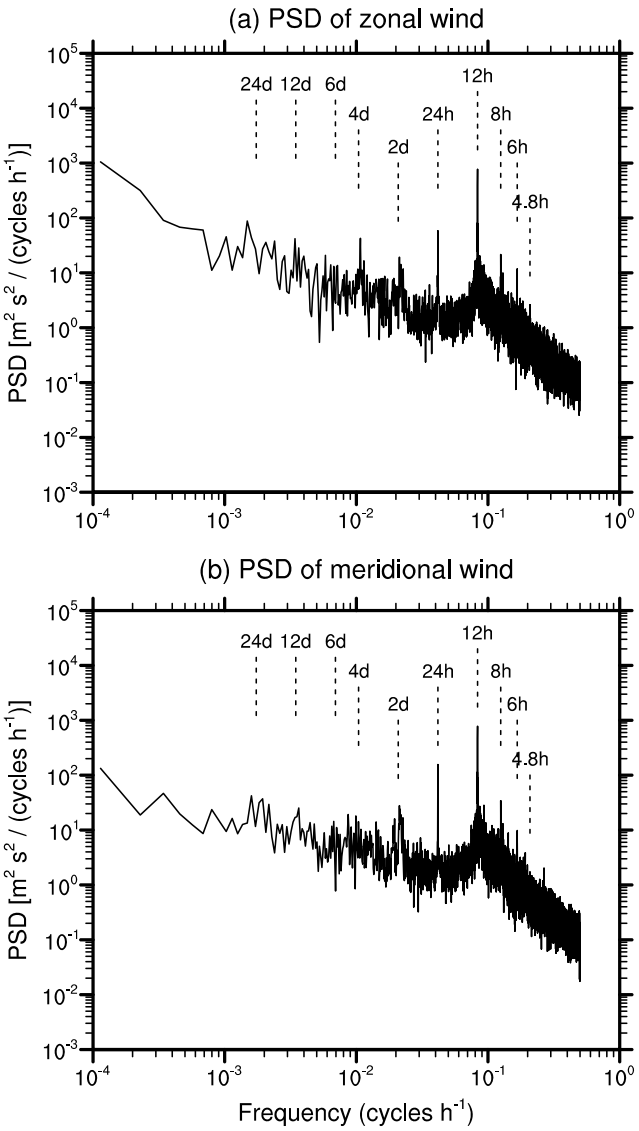

Figure 2. Vertically averaged power spectral densities (PSDs) of the hourly (a) zonal and (b) meridional wind components near the mesopause region over KSS for the whole year of 2014. PSDs computed at eight height bins (80, 84.5, 88, 90.5, 92.5, 95, 98.5, and 103 km) using the Lomb-Scargle periodogram method are interpolated in a regular frequency grid and then averaged in the vertical direction.

2.2. Methods to Retrieve GW Signals

Retrieval of GWs from meteor radar wind observations requires a finer spatiotemporal resolution than the resolution used to illustrate the spectral characteristics of the large-scale flow (section 2.1). For GW retrieval, the three-dimensional wind components are determined in regular time-height bins with the intervals of 2 min and 3 km for an altitude range of 78–105 km. As described in section 2.1, the three wind components are computed from meteor echoes observed within the zenith angles of 15°–60° using the least squares method, and the same rejection criteria are used. The least squares computation is carried out using meteor echoes detected within a 10 min time interval centered around each nominal 2 min bin and within a 3 km height interval around each 3 km bin. Using the smaller time (height) interval allows for detecting the more GWs with the shorter periods (vertical wavelengths), but it reduces the number of meteor echoes in each time (height) interval and as a result may damage the reliability of meteor radar wind itself. In this study, the 10 min and 3 km intervals are chosen, considering a trade-off between the reliability of wind data and the minimum resolvable period and vertical wavelength. The use of the 10 min interval makes the temporal resolution 20 min (Nyquist period). Owing to the vertically uniform height interval, the minimum resolvable vertical wavelength of GWs becomes a constant, independent of heights.

For GW retrieval, it is essential to properly identify the large-scale winds with tidal variations and filter them out in the time series at each height. For this, we employ 5 day time windows in the time series binned at the nominal interval of 2 min. Removal of the large-scale winds is achieved in each of the 5 day segments of the time series. The 5 day time window is stepped forward in time by 1 day until the end of observed data is reached, and GW retrieval, together with the removal of the large-scale winds, is also carried out in the 5 day time series. In each 5 day time series, GW signals are assumed to be fast varying in time (in the ground-based frame of reference), compared with the various global-scale waves shown in Figure 2. Therefore, separation of GW signals from the large-scale flow requires band-pass filtering. The use of the 5 day time window can be justified in that the rotation of tidal horizontal wind vectors with time [see *Andrews et al.*, 1987] is more clearly revealed when the extent of the time window used for the LS periodogram is longer than the 4 day time period that has been widely used in previous studies [e.g., *Mitchell et al.*, 2002; *Lee et al.*, 2013; *de Wit et al.*, 2014].

For band-pass filtering, the LS spectral analysis and Fourier reconstruction (synthesis) are carried out for each of 5 day time series binned at the nominal 2 min interval. Prior to the spectral analysis, we apply the Hann

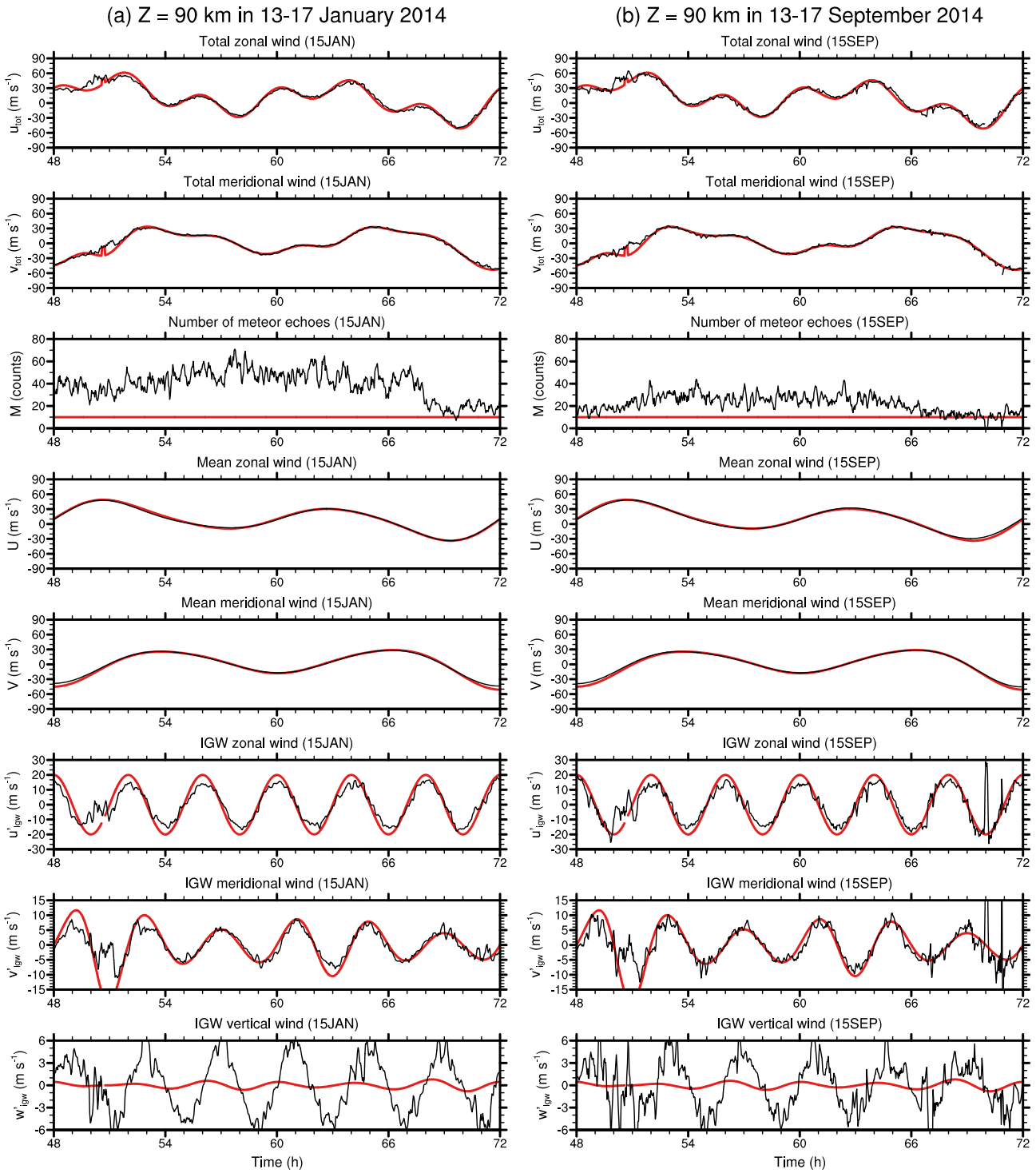

Figure 3. Time series of (black) meteor radar and (red) specified total horizontal wind components (rows 1 and 2) for meteor echo locations observed within the height range of 3 km around z = 90 km for 1 day in the middle of (a) 13–17 January and (b) 13–17 September (see the text for details). The number of meteor echoes within the same altitude range is plotted in the row 3, and the red line denotes the number 10. Time series of (black) the Fourier reconstructed and (red) specified large-scale horizontal wind components and three-dimensional IGW perturbation wind components are shown in the rows 4 and 5 and rows 6–8, respectively. In t = 50–51 h, the IGW amplitudes are set equal to zero when $\hat{\omega} < |f|$.

window function to each 5 day time series to minimize energy leak in the LS periodogram and to avoid endpoint contamination due to band-pass filtering [see *Press et al.*, 1992, chap. 13]. The ground-based periods of 4.5 h and 5.5 h are used as high-pass and low-pass cutoff periods, respectively, to extract GWs and the large-scale motions that include the four (24 h, 12 h, 8 h, and 6 h) tidal waves and planetary waves shown in Figure 2. That is, signals with ground-based periods smaller (larger) than 4.5 h (5.5 h) are considered as GWs (the large-scale flow). Further details on the cutoff periods are described in section 3.1. When the 5 day average of the number of meteor echoes within each 10 min interval (binned at the 2 min interval) is smaller than 10, the LS spectral analysis result is discarded, and the 5 day reconstructed time series is regarded as missing. The use of such a threshold for echo number allows for more reliable band-pass filtering (see Figure 3).

For reconstruction of the band-pass-filtered GW and large-scale signals in the time domain, phase functions for the LS periodograms are computed following *Hocke and Kämpfer* [2009]. The use of the Hann window function does not lead to any significant reduction in the magnitude of the reconstructed signals except for the time period of about 1.5 day near the both ends of the 5 day time series. Hence, in the following GW analysis, we employ the high-pass-filtered 30 h time series (1 day and additional 3 h time periods at both ends of the 1 day period) in the middle of each 5 day time period. Given that the 5 day time window is stepped forward in time by 1 day, partially overlapping GW signals, each of which is continuous on the 30 h segment, can be obtained throughout a whole year unless the LS periodograms are not computed due to the lack of meteor echoes.

3. Results

In most of meteor radar studies, GW activities have been estimated in a statistical sense by computing (co)variances of observed wind components in relatively broad time intervals such as 60–90 min [e.g., *Hocking*, 2005; *Fritts et al.*, 2010b; *Lee et al.*, 2013; *de Wit et al.*, 2014]. In this study, in contrast to the other studies, we make attempts to retrieve dominant quasi-monochromatic GW signals from the time series of meteor radar wind components (i.e., GWs present across a series of narrow 2 min time bins).

3.1. Test of GW Retrieval Method Using Specified Tidal and IGW Motions

First, we examine the potential of meteor radar observations for representing tidal and low-frequency IGW motions across a series of narrow time bins. We employ actual spatiotemporal distributions of meteor echoes and specify tidal and monochromatic IGW motions, using analytic formulas similar to those used by *Fritts et al.* [2010b], given as follows:

$$u(x,y,z,t) = u_m + u_d \sin(2\pi t/\tau_d) + u_{sd} \sin(2\pi t/\tau_{sd}) + u_{td} \sin(2\pi t/\tau_{td}) + u_{qd} \sin(2\pi t/\tau_{qd}) + u_{\mathrm{igw}} \cos\phi_{\mathrm{igw}}, \quad (1)$$

$$v(x,y,z,t) = v_m - v_d \cos(2\pi t/\tau_d) - v_{sd} \cos(2\pi t/\tau_{sd}) - v_{td} \cos(2\pi t/\tau_{td}) - v_{qd} \cos(2\pi t/\tau_{qd}) + v_{\mathrm{igw}} \sin\phi_{\mathrm{igw}}, \quad (2)$$

and

$$w(x,y,z,t) = w_{\mathrm{igw}} \frac{m\cos\phi_{\mathrm{igw}} + \alpha \sin\phi_{\mathrm{igw}}}{\sqrt{m^2+\alpha^2}}. \quad (3)$$

Here u_m and v_m are the mean zonal and meridional winds. (u_d, v_d), (u_{sd}, v_{sd}), (u_{td}, v_{td}), and (u_{qd}, v_{qd}) are the amplitudes of zonal and meridional wind components of 24 h (τ_d), 12 h (τ_{sd}), 8 h (τ_{td}), and 6 h (τ_{qd}) tidal wave motions, respectively. Considering the temporal variations of the semidiurnal tidal motions are significant especially near KSS in summer [e.g., *Murphy et al.*, 2003, 2006; *Akmaev et al.*, 2015], u_{sd} and v_{sd} are made to exhibit a 10 day amplitude modulation and assumed to be given by $u_{sd} = u_{sd0} f(t)$ and $v_{sd} = v_{sd0} f(t)$, respectively, where $f(t) = 1 + \sin^2(\pi t/(10\ \mathrm{day}))$. This tidal amplitude variation is equivalent to that at $z = 90$ km considered in the case 5 in *Fritts et al.* [2010b]. u_{igw}, v_{igw}, and w_{igw} denote the amplitudes of zonal, meridional, and vertical wind components of an IGW signal, respectively. $\alpha = 1/(2H)$. H is the atmospheric density scale height. ϕ_{igw} is the IGW phase function defined as $kx + ly + m(z - 90\ \mathrm{km}) - \omega t$. (k, l, m) is the three-dimensional IGW wave number vector, and ω is the ground-based IGW frequency.

From the PSDs shown in Figure 2, the amplitudes (m s^{-1}) of tidal waves are set as follows: $(u_d, v_d) = (10, 10)$, $(u_{sd0}, v_{sd0}) = (20, 20)$, $(u_{td}, v_{td}) = (5, 5)$, and $(u_{qd}, v_{qd}) = (3, 3)$ for $(u_m, v_m) = (10, 0)$. For the IGW signal, the eastward propagation is assumed ($k > 0$ and $l = 0$). The zonal wave number (k) and the ground-based frequency (ω) are set equal to $2\pi/(1000\ \mathrm{km})$ and $2\pi/(4\ \mathrm{h})$, respectively. Downward phase progression

($m < 0$ for $\omega > 0$) is assumed. The IGW amplitudes are determined based on the linear IGW theory [*Fritts and Alexander*, 2003]: $v_{igw} = (f/\hat{\omega})u_{igw}$ and $w_{igw} = -(k/\sqrt{m^2+\alpha^2})u_{igw}$ for a given u_{igw} (set equal to 20 m s^{-1}), where f is the Coriolis parameter at KSS; $\hat{\omega}$ is the intrinsic frequency given by $\omega - \mathbf{U}\cdot\mathbf{k}$; $\mathbf{U}$ is the large-scale horizontal wind vector; and $\mathbf{k}$ is the IGW horizontal wave number vector. The parameters $\hat{\omega}$ and m vary with time in a consistent way with the following IGW dispersion relation in the anelastic airflow system:

$$\hat{\omega}^2 = (\omega - \mathbf{U}\cdot\mathbf{k})^2 = \frac{N^2(k^2+l^2)+f^2(m^2+\alpha^2)}{k^2+l^2+m^2+\alpha^2}, \tag{4}$$

where N is the static stability (assumed to be 0.015 rad s^{-1}) and H is set equal to 7 km. Without loss of generality, $\hat{\omega}$ can be assumed to be positive. In fact, $|f| < \hat{\omega} < N$ from (4) for vertically propagating IGWs ($m^2 > 0$).

The vertical group velocity (c_{gz}) is given by $-(m/\hat{\omega})(\hat{\omega}^2-f^2)/(k^2+l^2+m^2+\alpha^2)$, and thus, m is negative (positive) for upward (downward) energy propagation since $\hat{\omega}$ is positive. The vertical phase velocity is given by ω/m, as can be seen in the phase ϕ_{igw} defined in (1)–(3), and therefore downward (upward) phase progression means sgn $(\omega/m) < 0$ (sgn $(\omega/m) > 0$). For the IGW in (1)–(3), the relation between the temporal rotation and vertical energy propagation direction is derived by defining the azimuth angle (ψ) of the IGW horizontal wind vector using the relation $\tan\psi = v'_{igw}/u'_{igw} = (f/\hat{\omega})\tan\phi_{igw}$ (where $u'_{igw} = u_{igw}\cos\phi_{igw}$ and $v'_{igw} = v_{igw}\sin\phi_{igw}$) and by differentiating this relation with respect to time for the slowly varying large-scale flow compared with IGW oscillations: $(\partial\psi/\partial t)\sec^2\psi \approx (-f\omega/\hat{\omega})\sec^2\phi_{igw}$. That is, the IGW horizontal wind vector rotates counterclockwise (clockwise) with time for sgn $(-f\omega) > 0$ (sgn $(-f\omega) < 0$). For upward energy propagation ($m < 0$), $\omega > 0$ ($\omega < 0$) indicates downward (upward) phase progression and counterclockwise (clockwise) rotation of the IGW horizontal wind vector in the Southern Hemisphere ($f < 0$). For downward energy propagation ($m > 0$), results are reversed, but such combinations are unlikely as the dominant GW sources are below the mesopause regions. For the above mentioned values of k, l, m (< 0) and ω (> 0) and the large-scale flow used in (1) and (2), $\hat{\omega}$ is found to be larger than $|f|$ in most of the time period except for a small time period (< 30 min) in 1 day when $\hat{\omega} < |f|$. Therefore, the specified IGW signal given above mostly represents an upward energy-propagating monochromatic IGW with downward phase progression. The amplitudes of the IGW are set equal to zero when $\hat{\omega} < |f|$.

Figure 3 shows the meteor radar winds for the specified motions given by (1)–(3) and their Fourier reconstruction obtained through the LS periodogram in the z = 90 km bin (88.5–91.5 km) for 1 day in the middle of 13–17 (5 days) January and September. The meteor radar winds for the specified motions mean the three-dimensional winds derived in the least squares sense from radial wind velocities computed from the specified motions defined using (1)–(3) at actual radar echo locations. It is found that the horizontal components of the three-dimensional winds of the specified motions at (x, y, z) = (0, 0, 90 km) are reasonably reproduced by the meteor radar winds for 1 day of 15 January and 15 September (rows 1 and 2 in Figure 3). Gaps in the meteor radar winds are mainly found in 18–24 UT (66–72 UT in Figure 3) regardless of seasons, due to sparse meteors during these hours in association with Earth's rotation and the movement of Earth around the Sun. As mentioned in section 2.1, meteor radar winds are not computed when the number of meteor echoes in each time-height bin is less than 7, but in many cases computed winds may be regarded as being unreliable when echo count is less than 10.

Figure 3 also shows the reconstructed large-scale and GW horizontal wind components. As mentioned in section 2.2, two separate ground-based cutoff periods (5.5 h and 4.5 h) are used to extract the large-scale and GW motions, respectively. Using the two separate cutoff values helps reduce undesirable interference between GWs and tidal motions near the 6 h ground-based period. An example of the interference is found when a single cutoff period of 5.5 h is used to extract both the large-scale motions and monochromatic IGWs with the ground-based periods of 4.5–5.5 h (see the cases for 4.77 h and 5.29 h in Figure S1 in the supporting information). Overall, for the two separate cutoff periods of 4.5 h and 5.5 h, the specified large-scale and IGW horizontal winds given by (1)–(3) are well represented by the reconstructed values. However, the IGW vertical wind case is problematic. The maximum value of the specified IGW vertical wind is about 1.2 m s^{-1}, while the magnitude of the reconstructed IGW vertical wind amounts to more than 6 m s^{-1}. This large discrepancy is likely due to the vertical projection of errors in the large-magnitude horizontal wind in the matrix equation used to obtain wind components from radar echoes in the least squares sense [*Hocking and Thayaparan*, 1997]. For this reason, vertical velocities are considered unreliable throughout this study and not used in the GW analysis.

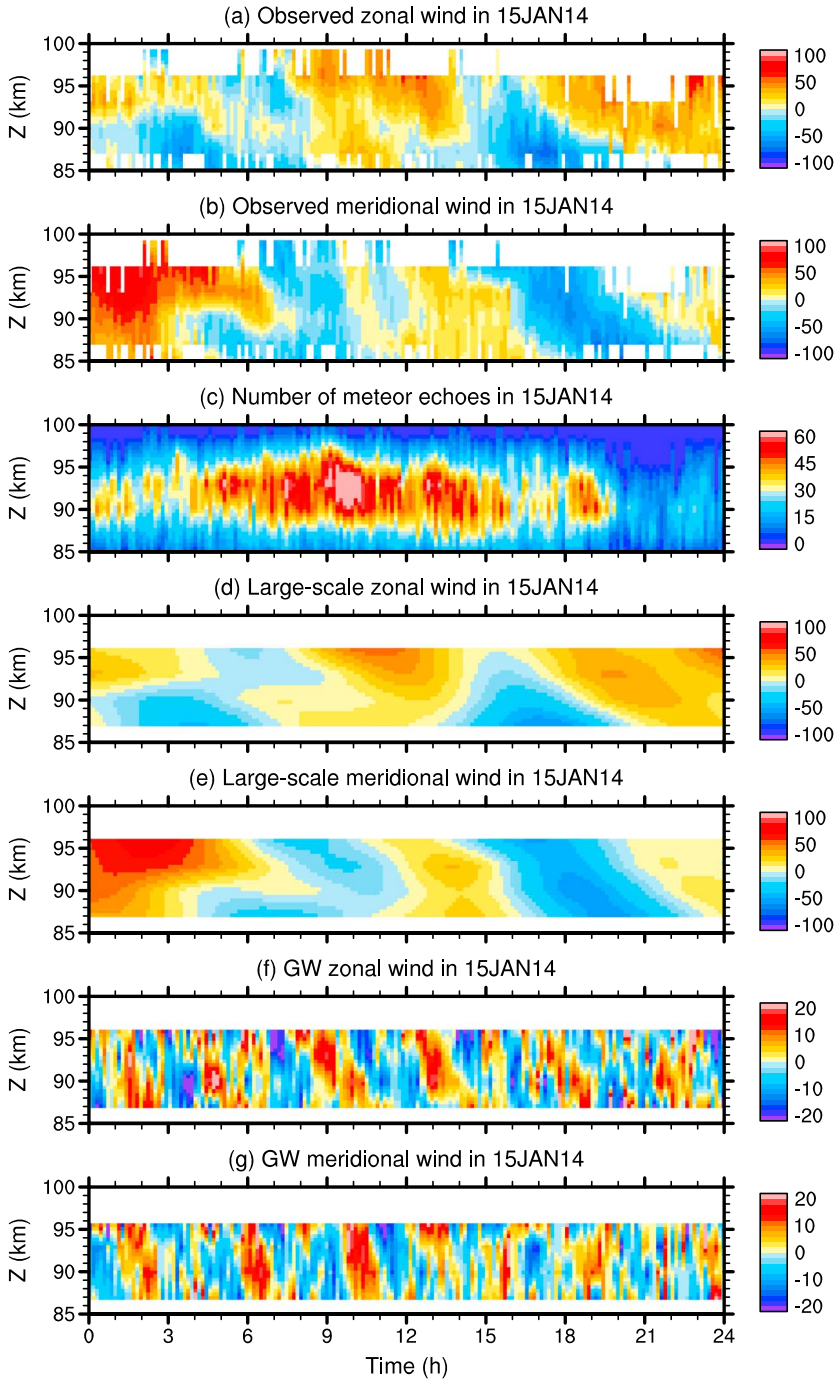

Figure 4. Time-height cross sections of meteor radar observed (a) zonal and (b) meridional wind components, (c) the number of meteor echoes, the large-scale (d) zonal and (e) meridional wind components, and GW (f) zonal and (g) meridional wind components in 15 January 2014.

3.2. General Characteristics of GWs Over KSS in 2014

Figure 4 demonstrates time-height cross sections of observed horizontal winds, the number of meteor echoes, and reconstructed large-scale and GW horizontal wind components for 15 January 2014. Meteor radar horizontal wind components (Figures 4a and 4b) have valid values when the number of meteor echoes within each time-height bin is roughly larger than 10 (Figure 4c). The large-scale horizontal wind components (Figures 4d and 4e) computed from the LS periodogram reasonably capture the slowly varying time-height variations of

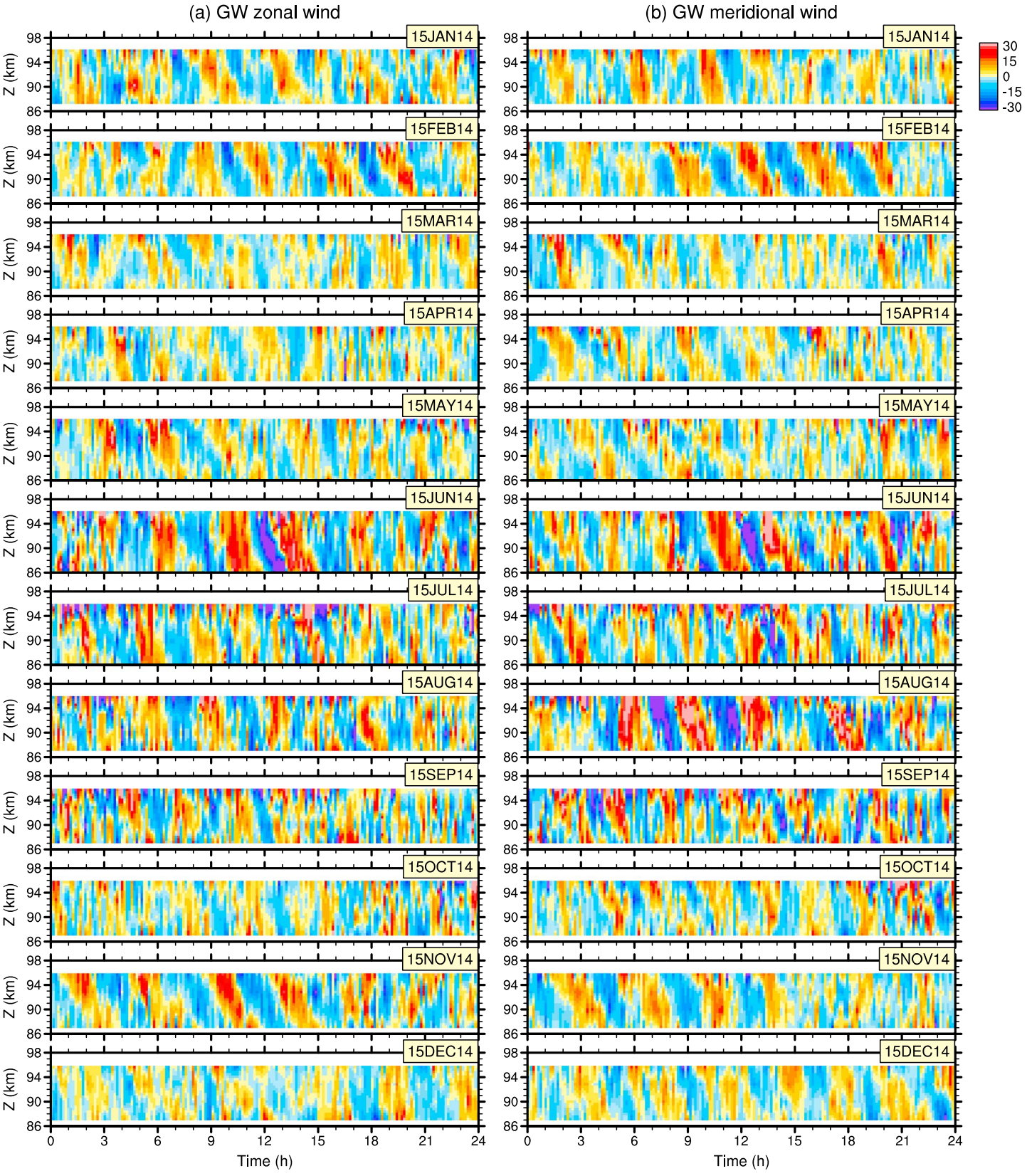

Figure 5. Time-height cross sections of GW (a) zonal wind and (b) meridional wind components for the fifteenth day of each month in 2014.

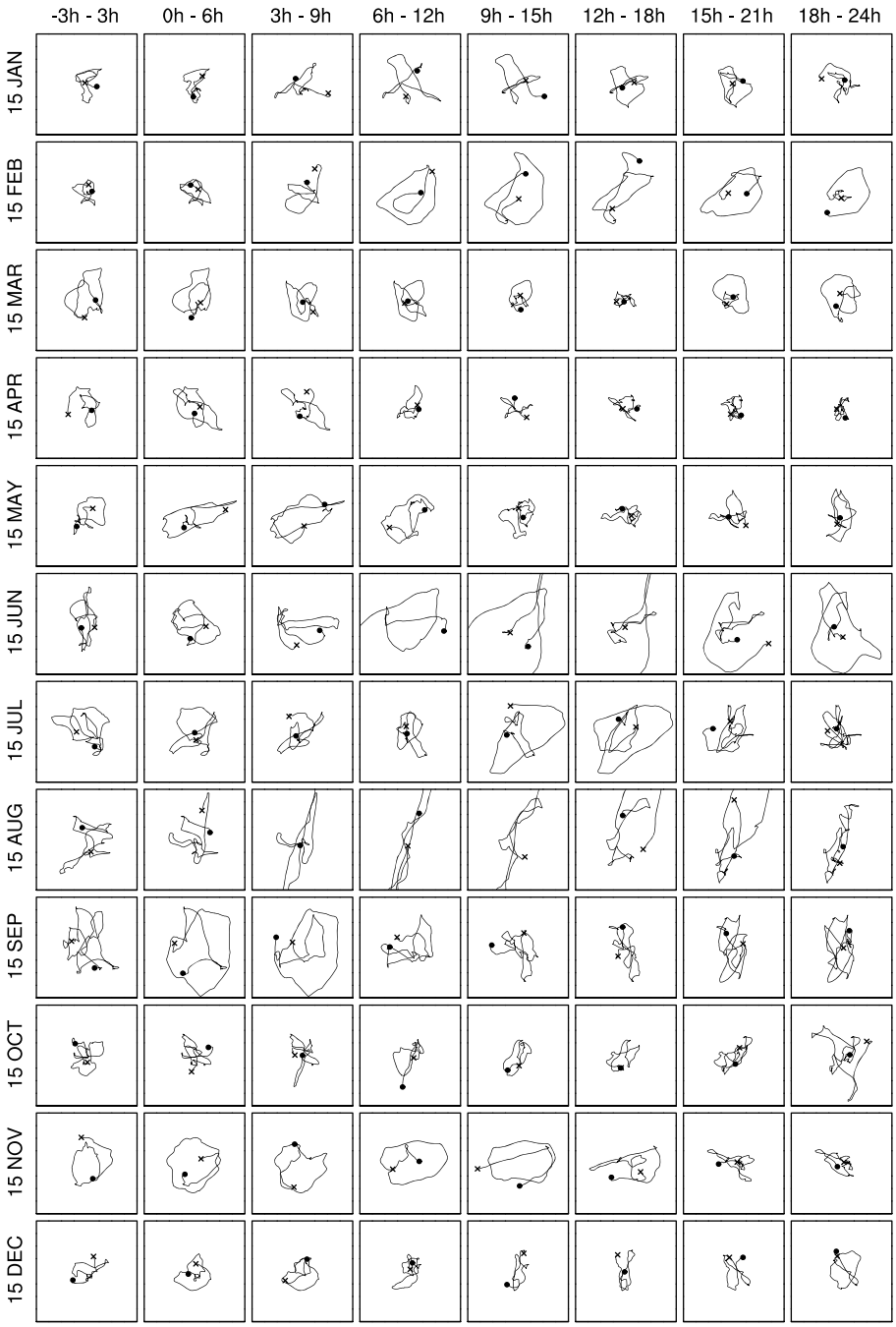

Figure 6. Hodographs of GW horizontal wind components (u'_{gw} and v'_{gw}) at z = 93 km in eight overlapping 6 h time windows for the fifteenth day of each month in 2014. Filled circles and cross denote starting and end points in time, respectively. Each hodograph is moving averaged for illustration purpose and plotted in the two-dimensional (u'_{gw} – v'_{gw}) domain of which each axis ranges from −30 to 30 m s^{-1}.

the observed horizontal wind components. In this large-scale flow, semidiurnal variations are dominant, consistent with the PSDs of the hourly winds shown in Figure 2.

The GW horizontal wind components (Figures 4f and 4g) exhibit downward phase progression with the vertical wavelengths of 15 km or larger. The downward phase progression seems to be related to the upward IGW energy propagation. Note that for upward energy propagation, the horizontal wind components of IGWs with downward phase progression should exhibit a counterclockwise rotation in time. Figures 4f and 4g qualitatively demonstrate such a counterclockwise rotation. For example, it is seen around z = 93–96 km at

t = 9–11 h and t = 1–3 h that GW zonal wind component precedes in time its meridional component by about 1–2 h. This phase difference is consistent with the elliptical polarization of IGW horizontal wind vector.

The characteristics of the IGW winds in the time-height cross section mentioned above seem to be frequently found over KSS for any parts of the 1 year time period. Figure 5 shows the time-height cross sections of the GW zonal and meridional wind components in the fifteenth day of each month in 2014. Vertical wavelengths range from 15 km (e.g., meridional components at t = 12.5 h in 15 February) to more than 20 km (e.g., meridional components at t = 10 h in 15 January), considering that the half wavelength of the vertical oscillation looks similar to or larger than 8–9 km. Detection of GWs with the vertical wavelengths larger than about 15 km may not necessarily mean the predominance of such GWs in the polar mesopause region, but it is more likely due to the use of the 3 km height bin. As also shown in Figure 4, downward phase propagation is predominant, and phase difference in time between the two wind components is easily found in several portions of the 1 day time period in each month (e.g., t = 9–12 h in 15 February, t = 3–6 h in 15 May, and t = 9–12 h in 15 November).

For any chosen days in each month, we may find similar downward phase progression and phase difference between GW zonal and meridional wind components, which suggests frequent occurrence of upward energy-propagating IGWs in the southern polar mesopause region. The occurrence rate of IGWs can be quantified by counting events during which parameters related to the elliptical polarization of IGWs exceed certain criteria. The event counting indicates that coherent and upward energy-propagating IGW signals can be found in about 34% of the 1 year time period. The occurrence rate is increased up to 65% when partially coherent waves are included. Details on polarization and event counting are given in sections 3.3 and 3.4, respectively.

Figure 6 demonstrates the temporal hodographs of the GW horizontal wind components in the z = 93 km bin (91.5–94.5 km) for the fifteenth day of every month in the year 2014. The 1 day time series (actually, the 27 h time series from −3 h to 24 h) shown in Figure 5 is subdivided into eight overlapping 6 h time segments. For each of the 6 h time segments, the hodograph of the GW horizontal wind components is plotted. The use of the eight subdomains at a 3 h interval enables us to consider Doppler shifting effects due to the strong diurnal and semidiurnal tides (see Figure 2) in that the 3 h interval can resolve semidiurnal oscillations. It is seen from Figure 6 that the hodographs mostly rotate counterclockwise in time except for some cases when their hodographs are either extremely noisy or highly anisotropic. The predominance of the counterclockwise rotation means that most of the observed GWs in the southern polar mesopause region are IGWs that may transport their energy upward. The major axis direction of the elliptical shape of the hodographs gives the horizontal IGW propagation direction, albeit with 180° ambiguity [*Andrews et al.*, 1987]. This property has been employed in a number of observational studies based on radars [e.g., *Vincent and Fritts*, 1987; *Vincent and Eckermann*, 1990; *Sato*, 1993; *Chen et al.*, 2013] and radiosondes [e.g., *Eckermann*, 1996; *Wang et al.*, 2005; *Chun et al.*, 2006; *Moffat-Griffin et al.*, 2011, 2013; *Murphy et al.*, 2014] to understand IGW propagation characteristics. Quick examination of Figure 6 reveals that the major axes of the hodographs roughly lie in the N-S or NW-SE direction in January, February, and December and in the NE-SW or ENE-WSW direction in May, June, July, and August.

3.3. Quantitative Hodograph Analysis Based On the Stokes Parameter Method and Rotary Spectra

For quantitative understanding, we employ the Stokes parameter method for the GW horizontal wind hodograph in each of the 6 h time segments for every day throughout the 1 year period of 2014. The Stokes parameter method is originally devised to analyze the polarization of electromagnetic waves [*Born and Wolf*, 1999]. *Vincent and Fritts* [1987] first employed this method to obtain IGW propagation properties from MF-radar wind observations. Stokes parameters are composed of four values that describe the polarization state of a monochromatic wave, and the four parameters are often denoted by I (the throughput), D (the throughput anisotropy), P (the linear polarization), and Q (the circular polarization).

In this study, similar as in *Eckermann* [1996], we compute spectrally averaged Stokes parameters using the Fourier coefficients for each 6 h time series of GW horizontal wind components (u'_{gw} and v'_{gw}) (e.g., see hodographs in Figure 6), assuming that GW fields are in general mixture of various monochromatic waves. In the frequency domain, the four parameters I, D, P, and Q are given by

$$I = \overline{\left|\hat{u}_{gw}(\omega)\right|^2} + \overline{\left|\hat{v}_{gw}(\omega)\right|^2}, \tag{5}$$

$$D = \overline{\left|\hat{u}_{gw}(\omega)\right|^2} - \overline{\left|\hat{v}_{gw}(\omega)\right|^2}, \tag{6}$$

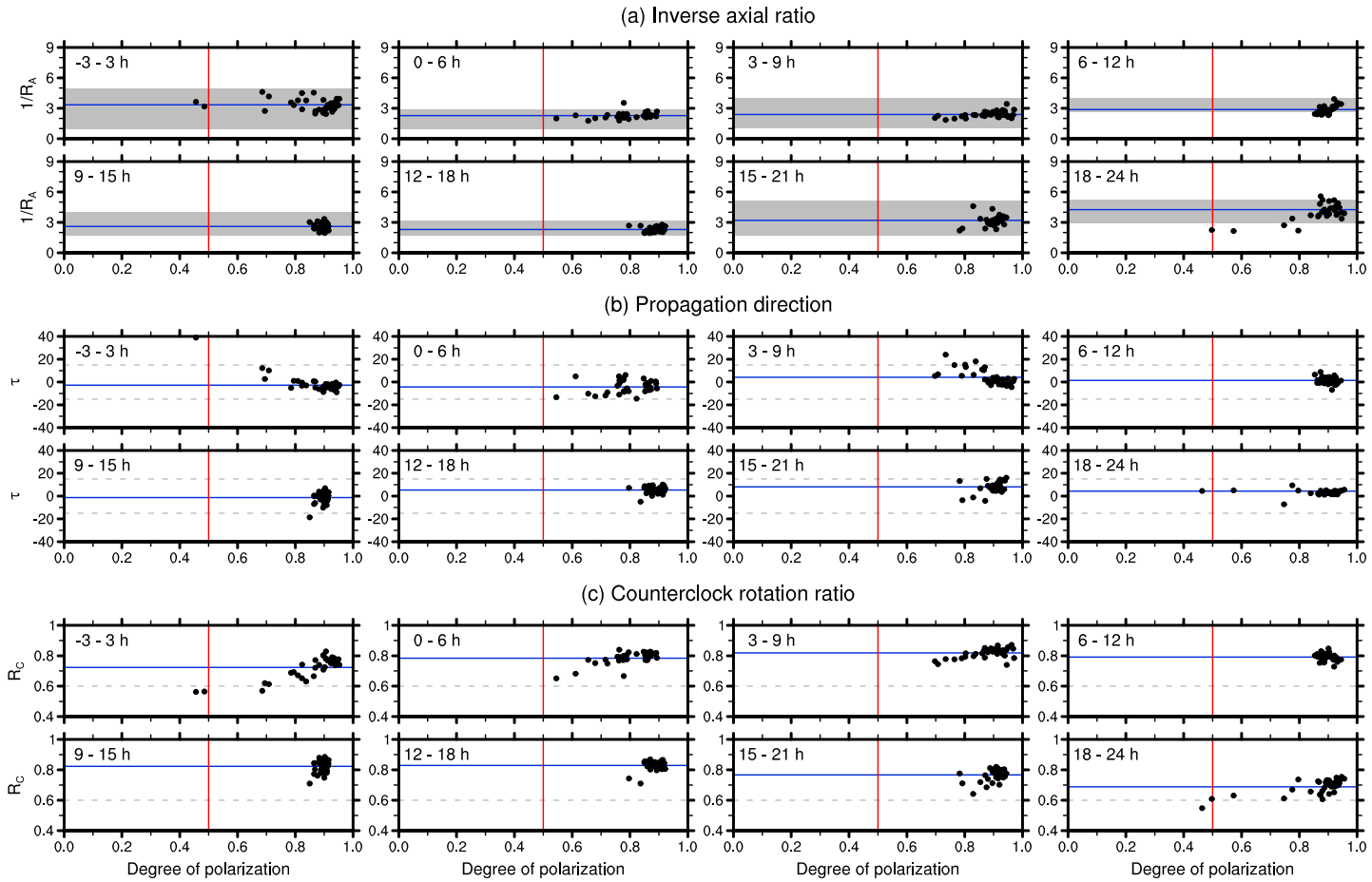

Figure 7. Scatterplots of (a) inverse axial ratio (R_A^{-1}), (b) propagation direction (τ), and (c) counterclockwise rotation ratio (R_C) as a function of the degree of polarization (d). Each panel is plotted for one of the eight time (6 h) segments in the GW time series extracted from the meteor radar winds for the specified motions given in (1)–(3). Meteor radar winds are obtained for actual echo locations within $z = 85.5–94.5$ km for the fifteenth day of all months in 2014. In Figure 7a, the theoretical range of the intrinsic frequency is plotted in gray shading for each 6 h segment. The blue line indicates the 6 h averaged value of each parameter. The red line denotes the value of $d = 0.5$.

$$P = 2\overline{\mathrm{Re}\left[\hat{u}^*_{\mathrm{gw}}(\omega)\hat{v}_{\mathrm{gw}}(\omega)\right]}, \tag{7}$$

and

$$Q = 2\overline{\mathrm{Im}\left[\hat{u}^*_{\mathrm{gw}}(\omega)\hat{v}_{\mathrm{gw}}(\omega)\right]}, \tag{8}$$

where $\hat{u}_{\mathrm{gw}}$ and $\hat{v}_{\mathrm{gw}}$ are the Fourier coefficients of the GW zonal and meridional wind components, respectively, the superscript $*$ denotes the complex conjugate, and the over bar is the averaging operator in the frequency domain.

The degree of polarization (d) defined as $\sqrt{D^2+P^2+Q^2}/I$ is a useful parameter that measures the ratio of the polarized portion in a given mixture of monochromatic IGWs. Pure monochromatic waves are perfectly polarized ($d = 1$), and perfectly random waves are completely incoherent ($d = 0$). Using (5)–(8), we can obtain the direction (τ) of the major axis of hodograph and the ratio of the minor axis to the major axis (called the axial ratio R_A):

$$2\tau = \arctan(P/D), \tag{9}$$

$$2\xi = \arcsin(|Q/(d \cdot I)|), \tag{10}$$

and

$$R_A = \tan(\xi). \tag{11}$$

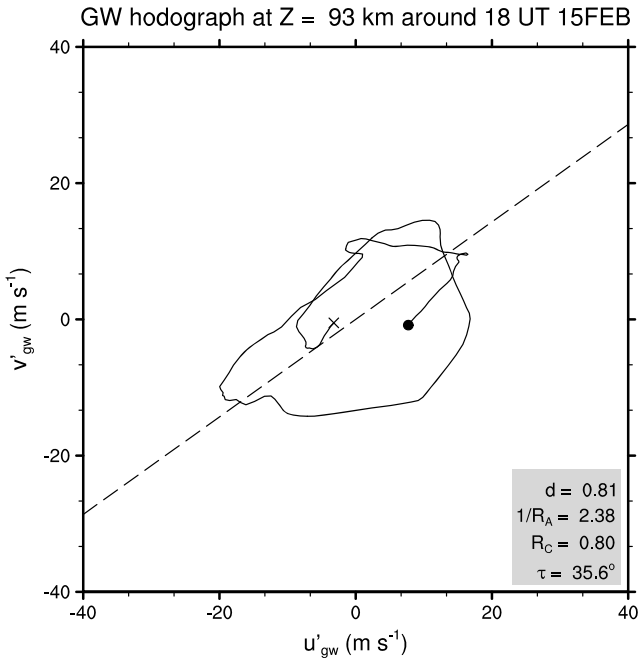

Figure 8. GW horizontal wind hodograph (thin solid line) at z = 93 km for a 6 h time period around 18 UT in 15 February and GW parameters (d, R_A^{-1}, R_C, and τ) estimated from the hodograph. Dashed line denotes the major axis direction represented by the value of τ. GW parameters are computed using unsmoothed wind values, while the hodograph plotted here is moving averaged in time for better illustration.

The intrinsic frequency $\hat{\omega}$ is determined from the axial ratio $R_A(|f|/\hat{\omega}; 0 < R_A \leq 1)$. In this computation of $\hat{\omega}$ from R_A, we ignore effects of the vertical shear of the large-scale flow perpendicular to the GW horizontal wave number vector [*Hines*, 1989] since the direction of GW horizontal wave number vector cannot be determined in an unambiguous way in this study where only horizontal winds are employed without additional variables such as temperature or density. As discussed by *Sato and Yoshiki* [2008], the wind shear effects can be important for linearly polarized GWs with very small R_As in the large-scale flow with large vertical wind shear, but they may not be significant in our case, considering that the magnitude of the vertical wind shear averaged in the 6 h time period, in which the R_A is estimated, is $O(10^{-5}) - O(10^{-3})$ s^{-1}. In fact, using (6) in *Sato and Yoshiki* [2008], it can be shown that the wind shear effects are not significant for such a shear magnitude of $O(\leq 10^{-3})$ as long as the vertical to horizontal wavelength ratios of GWs (λ_z/λ_h) are $O(\leq 10^{-1})$.

The ratio of counterclockwise rotation (R_C) is another important parameter and is obtained by computing the rotary spectra of the complex wind time series ($u'_{gw} + iv'_{gw}$) [*Eckermann*, 1996] and then by measuring the ratio of powers at counterclockwise frequencies ($\omega > 0$) to total power. Both rotation sense and polarization can influence the value of R_C, but values greater than 0.5 suggest counterclockwise rotation. This in turn indicates upward energy propagation for the downward phase progression in the Southern Hemisphere as mentioned in section 3.1.

Estimation of the parameters d, R_A^{-1}, τ, and R_C through Stokes parameter method and rotary spectra is tested using meteor radar winds for the specified motions given in (1)–(3) (see Figure 3). For a larger sample size, meteor radar winds in this test are obtained for the fifteenth day of all months including 2 months shown in Figure 3. Stokes parameters and rotary spectra are computed for each 6 h segment in the 30 h time series, as shown in Figure 6. Figure 7 demonstrates the parameters R_A^{-1}, τ, and R_C as a function of d at z = 87, 90, and 93 km bins for 12 months. Results at $z < 85.5$ km or $z > 94.5$ km are not included since they are occasionally scattered too much around theoretical values, which seems to be related to sparse meteors at these heights. Hence, parameters in the three height bins of 87, 90, and 93 km are mainly discussed hereafter.

Figure 7 confirms that the intrinsic frequencies ($\hat{\omega}$) estimated from R_A^{-1} are reasonably found within the analytic range (gray shading) for each 6 h time interval. The analytic range is given by the variation of $\omega - Uk$ during the 6 h interval, where U is the large-scale zonal wind obtained through the low-pass filtering. The propagation direction (τ) roughly ranges from −15° to 15° around the theoretical value 0°, which implies that an error range for τ caused by our method may be ±15°. The counterclockwise rotation ratios (R_C) are found to be roughly larger than 0.6 in spite of the pure upward energy propagation of the specified IGW. Figure 7 also illustrates that reasonable agreement between estimated parameters and theoretical values is found roughly for $d > 0.5$ and $R_C > 0.6$. This result indicates that the two criteria ($d > 0.5$ and $R_C > 0.6$) can in turn be used to examine if observed GWs with downward phase progression can be regarded as coherent, quasi-monochromatic, and upward energy propagating IGWs.

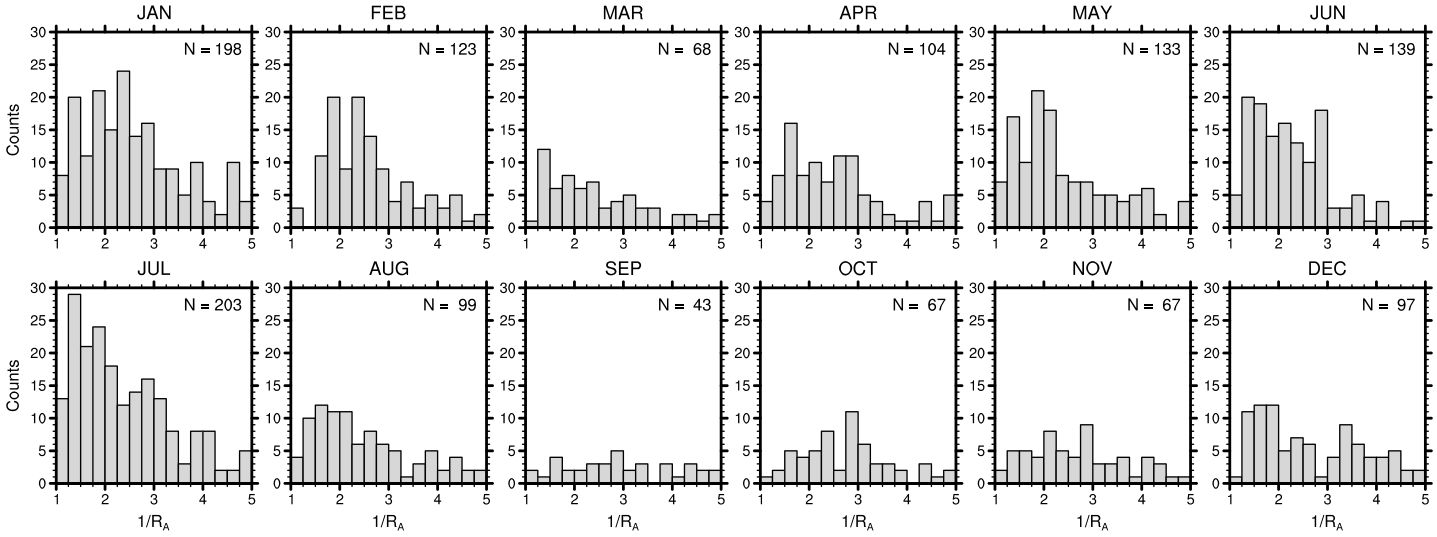

Figure 9. Monthly histograms of GW intrinsic frequencies relative to the Coriolis parameter in the mesopause region (z = 85.5–94.5 km) over KSS. The histograms are made for coherent and upward energy-propagating GW events. The number of coherent and upward energy propagating GW events is plotted in each panel for each month.

Figure 8 shows an example of the estimated parameters (d, R_A^{-1}, τ, and R_C) for the GW horizontal wind hodograph in the 6 h time period at z = 93 km around 18 UT in 15 February 2014. The hodograph shown in Figure 8 represents highly coherent IGW perturbations as indicated by the high value (0.81) of the degree of polarization. The inverse axial ratio R_A^{-1} of 2.38 looks reasonable when judged from the overall elliptical shape of the hodograph. The hodograph exhibits counterclockwise rotation in time, which is consistent with R_C = 0.8. The estimated propagation angle measured counterclockwise from the due east is 35.6°, and it corresponds reasonably well to the major axis direction of the hodograph. The IGW parameters computed from Stokes parameters in this study generally pass the graphical sanity check as shown here (not shown in detail).

3.4. Estimation of GW Intrinsic Frequencies, Group Velocities, and Propagation Directions

Figure 9 shows histograms of intrinsic frequencies for coherent ($d > 0.5$) and upward energy-propagating GWs ($R_C > 0.6$) within $z = 85.5 - 94.5$ km. As described in section 3.3, the intrinsic frequencies are computed from the GW signals in individual 6 h time periods (overlapping eight time sectors in each day). Events of coherent GWs ($d > 0.5$) with $R_C > 0.6$ within the altitude range of 85.5–94.5 km are counted. Any occurrence of such events within the height range is regarded as one event for a given 6 h time period. An occurrence rate is computed by dividing the total number of events by the number of 6 h time intervals. The use of the overlapped time intervals may not lead to an increase in the occurrence rate because the numbers of events and time intervals may be increased by similar amounts. In this way, the events of coherent GWs with $R_C > 0.6$ are found in about 34% of the 1 year time period (i.e., 34% among 8 × 365 time sectors), which suggests frequent occurrence of quasi-monochromatic and upward energy-propagating IGWs. For those events, $\hat{\omega}$ is found to be generally smaller than $5|f|$. *Vincent and Fritts* [1987], however, found that observed gravity waves near mesopause regions are, in fact, partially coherent, and the values of d are about 0.2 or less. Therefore, if events of partially coherent waves are considered by lowering the criteria for d from $d > 0.5$ to $d > 0.2$ and by retaining criteria for R_C, the occurrence frequency becomes about 65%, which is more consistent with the evident persistence of gravity waves with downward phase progression (Figure 5).

In Figure 9, it is interesting that GWs are found to be dominant at $\hat{\omega} = |f| - 3|f|$ regardless of seasons. Relative predominance between the two intrinsic frequency ranges of $|f| - 2|f|$ and $2|f| - 3|f|$ varies on a seasonal time scale, with the more GW events with $2|f| - 3|f|$ in austral summer (January and February) and the more events with $|f|$–$2|f|$ in austral autumn and winter (May–July). IGW packets propagate with the elevation slope approximately given by $|\mathbf{k}|/|m|$ $(= \sqrt{\hat{\omega}^2 - f^2}/N)$ in the frame of reference that moves at the same velocity as the background wind projected in the IGW wave number direction [*Andrews et al.*, 1987]. That is, observed GW packets with low intrinsic frequencies propagate relatively short vertical distance for a given horizontal distance in the moving frame of reference.

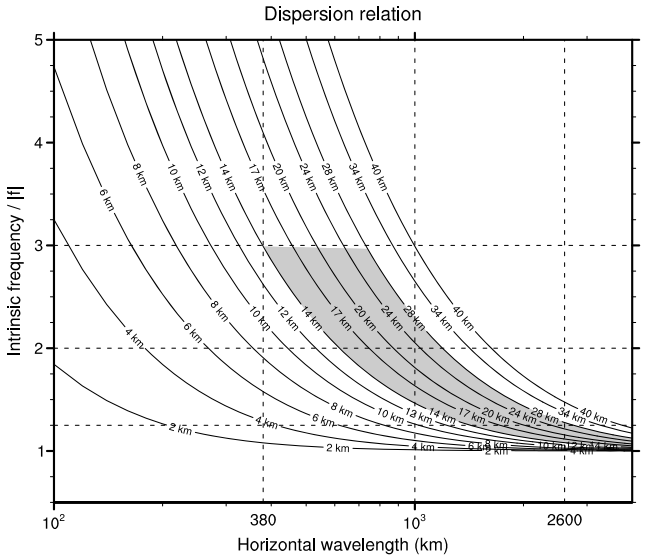

Figure 10. IGW dispersion relation curves as a function of horizontal wavelength for the vertical wavelengths from 2 km to 40 km. The area of horizontal wavelengths for intrinsic frequencies of $|f|-3|f|$ and vertical wavelengths of 14–28 km are shaded.

Knowledge of GW vertical and horizontal wavelengths together with horizontal propagation direction enables us to infer the trajectories of observed GW packets. In this study, for the given range of dominant intrinsic frequencies and vertical wavelengths, it is possible to estimate approximate ranges of horizontal wavelengths. Figure 10 illustrates the dispersion relation curves (4) plotted as a function of the horizontal wavelengths (λ_hs) for the vertical wavelengths (λ_zs) of 2–40 km. The λ_z range of 14–28 km is highlighted. This λ_z range is chosen based on Figures 4 and 5 and consistent with the previous studies on the southern polar mesospheric IGWs (16 km in *Suzuki et al.* [2013b], 22–23 km in *Chen et al.* [2013], and 20–30 km in *Chen et al.* [2016]). For GWs with $\hat{\omega} = 2|f| - 3|f|$, the GWs are expected to have the λ_hs of about 400–1000 km. For $\hat{\omega} = |f|-2|f|$, λ_h can range roughly from 700 to 3000 km for $\lambda_z = 14$–28 km.

These results indicate that GWs retrieved in this study are IGWs with large λ_hs in contrast to small-scale mesospheric GWs with λ_hs < 100–200 km that have been dealt with in previous radar studies [e.g., *Reid and Vincent*, 1987b; *Hocking*, 2005]. Quick computation of group velocities given in an approximated form ($c_{gh} = U + N^2|\mathbf{k}|/(m^2\hat{\omega})$ and $c_{gz} = N^2|\mathbf{k}|^2/(|m|^3\hat{\omega})$) for $N = 0.015$ rad s^{-1}, $\hat{\omega} = 2|f|$, $|\mathbf{k}| = 2\pi/(1000$ km), and $|m| = 2\pi/(20$ km) yields $c_{gh} \approx 4800$ km d^{-1} and $c_{gz} \approx 96$ km d^{-1} when the background wind projected into the IGW propagation direction is assumed negligible. Based on Figure 10, for $\hat{\omega} = 1.5|f|$ and $|\mathbf{k}| = 2\pi/2000$ km, $c_{gh} \approx 3200$ km d^{-1} and $c_{gz} \approx 32$ km d^{-1}. For $\hat{\omega} = 2.5|f|$ and $|\mathbf{k}| = 2\pi/700$ km, $c_{gh} \approx 5500$ km d^{-1} and $c_{gz} \approx 160$ km d^{-1}. IGWs with $\hat{\omega} = 2|f|-3|f|$ can propagate relatively long vertical distance for a given horizontal distance, compared to those with $\hat{\omega} = |f|-2|f|$. If we assume IGW sources located similar horizontal distance from KSS, IGWs with $\hat{\omega} = 2|f|-3|f|$ could emanate from the troposphere, and those with $|f|-2|f|$ from the stratosphere, considering the estimated c_{gh} and c_{gz}.

Figure 11 shows the angular histograms for the horizontal propagation directions of coherent GWs ($d > 0.5$) with $R_C > 0.6$ as shown in Figure 9. The propagation direction has the 180° ambiguity, and thus, the histogram is symmetric with respect to 180° rotation. The horizontal propagation directions of mesospheric GWs observed over KSS exhibit clear seasonal variations. In summer (January, February, and December), the N-S propagation is generally predominant, while in winter (June–August), NE-SW propagation becomes more pronounced. In autumn (March–May), results are overall similar to winter. In spring (September–November), a gradual change from the NE-SW propagation to the N-S propagation is found.

Small-scale, high-frequency GWs observed from all-sky camera images at $z = 86$ and 95 km over KSS for March–October in 2008–2015 indicate that the NW and SW propagation is dominant [*Kam et al.*, 2016]. When compared with this result for high-frequency GWs, it is interesting that the NW propagation detected in the all-sky images is not often found in the angular histograms for March–October shown in Figure 11. Although detailed comparison is beyond the scope of this study, the discrepancy might be attributed to different source mechanisms. Considering that high-frequency GWs may propagate far more in the vertical direction compared with the low-frequency IGWs, those high-frequency GWs may possibly be locally generated in regions close to KSS. Meanwhile, the low-frequency IGWs can be generated by sources located far from KSS. Generation of IGWs will be further discussed in the next section.

The N-S propagation is reminiscent of the southward and upward propagating IGWs near the polar stratopause level that were inferred from GW variances obtained from the Microwave Limb Sounder (MLS)

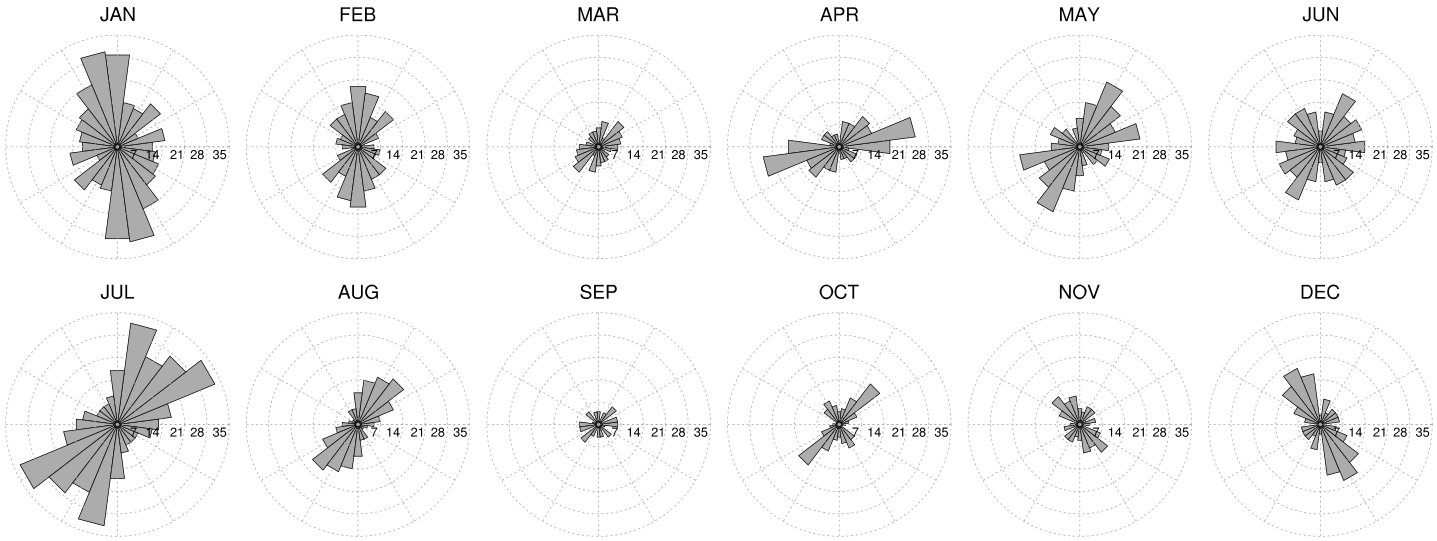

Figure 11. Monthly angular histograms of the horizontal propagation directions (z = 85.5–94.5 km) of GWs observed in the mesopause region over KSS. Angular histograms are symmetrical with respect to 180° rotation.

on the Aura satellite and European Centre for Medium-Range Weather Forecasts (ECMWF) Integrated Forecast System temperature analysis fields [*Wu and Eckermann*, 2008]. *Wu and Eckermann* [2008] discussed that these southward (i.e., poleward) propagating GWs may be IGWs that are spontaneously generated from the tropospheric jet flow in association with the instabilities of the baroclinic system. In ECMWF analysis shown in their Figure 10, IGWs that emanated from the strong jet flow areas over the Southern Ocean are found to exhibit almost zonally aligned phase lines along the coastlines of Antarctica. Although the ECMWF temperature was filtered so that it can only resolve IGWs with λ_hs < 300 km and λ_zs > 6 km for comparison with the MLS, the ECMWF analysis clearly shows that the jet front system can act as a source of the GWs that primarily propagate southward from the Southern Ocean to the South Pole.

4. Generation of IGWs

The spontaneous generation of IGWs in association with the baroclinic system has been extensively studied for more than two decades [see *Plougonven and Zhang*, 2014]. *Uccelini and Koch* [1987] reported, by reviewing IGW events, that the generation of IGWs is typically found near tropospheric jet exit regions. *O'Sullivan and Dunkerton* [1995] numerically reproduced the generation of IGWs with small intrinsic frequencies ($\hat{\omega} = |f| - 2|f|$) at jet exit regions. The spontaneous generation has been considered to be closely related to imbalances in the jet flow, and the location of the imbalance has been identified with Lagrangian (or local) Rossby numbers ($Ro = |\zeta/f|$, where ζ is the relative vorticity) [e.g., *Plougonven et al.*, 2003; *Sato and Yoshiki*, 2008] or a more sophisticated indicator (ΔNBE) associated with nonlinear imbalance [*Zhang et al.*, 2001; *Zhang*, 2004] given by

$$\Delta\mathrm{NBE} = 2J(u,v) + f\zeta - \nabla^2\Phi - \beta u, \tag{12}$$

where $J(u,v)$ is the Jacobian of the first-order derivatives of u and v, Φ is the geopotential, and $\beta = \partial f/\partial y$.

In this section, we employ the ΔNBE indicator, together with the *Ro* (Figures S2 and S3) in the supporting information, computed using the ECMWF Re-Analysis (ERA) Interim (ERA hereafter) data [*Dee et al.*, 2011] to examine the spontaneous generation of IGWs in jet flow systems. Possibilities of generation from other sources will be discussed thereafter. Figure 12 shows the monthly averaged nonlinear imbalance term and horizontal wind speed at 200 hPa throughout the year 2014. The horizontal structure of the wind speed generally agrees well with that of the monthly averaged eastward flow at 200 hPa (not shown). Tropospheric jet flows in the Southern Hemisphere show clear seasonal variations in their location and strength. From late spring (November) to midautumn (April) tropospheric jets mainly appear in the latitude range of 45°S–60°S, while from late autumn (May) to midspring (October) tropospheric jet systems appear separately as the strong

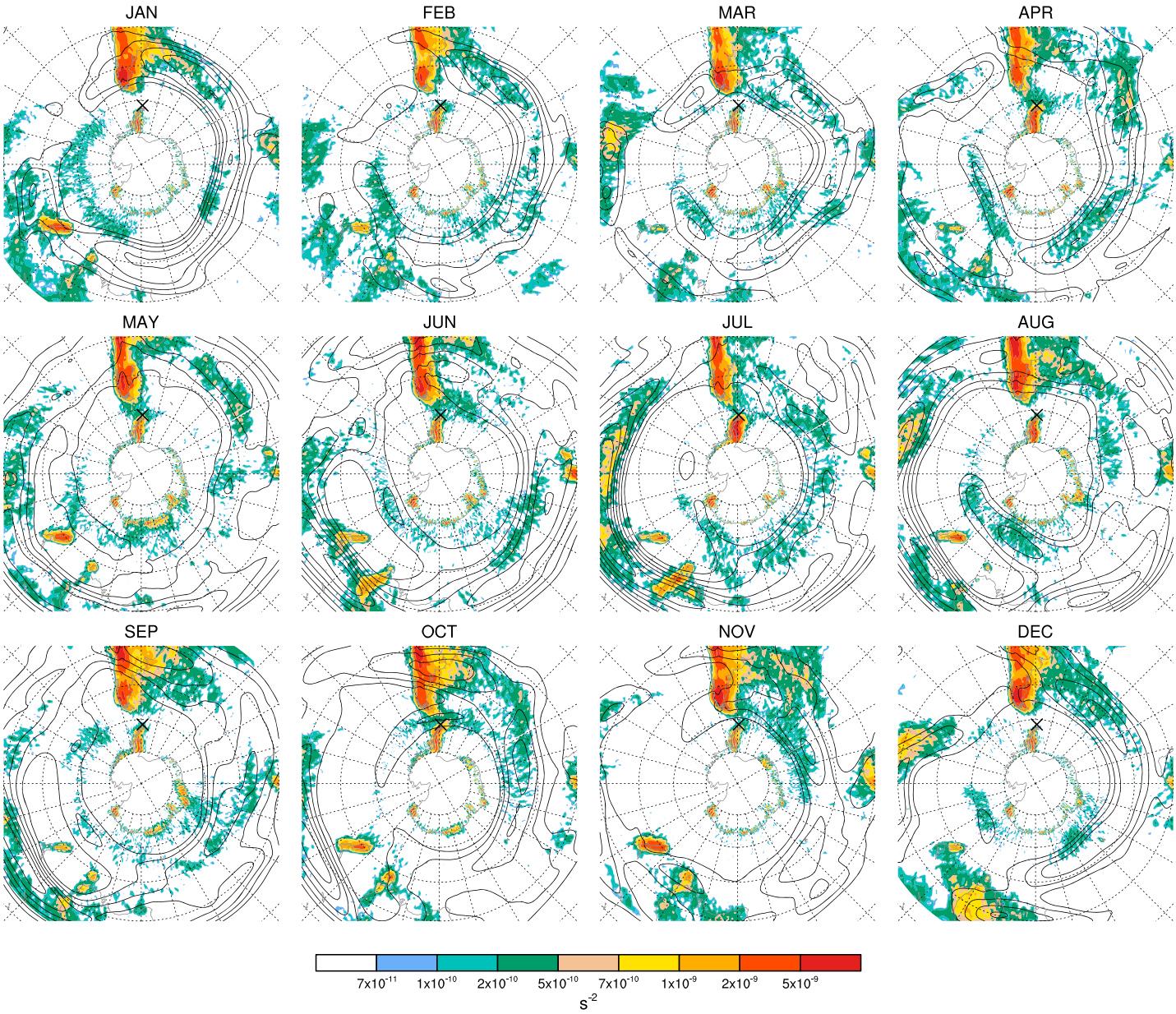

Figure 12. Monthly mean |ΔNBE| (shading) and horizontal wind magnitude (solid line: 30, 35, 40, 45, 50, 55, and 60 m s^{-1}) at 200 hPa. Zonal mean of the monthly mean |ΔNBE| is removed to clearly illustrate its longitudinal variation. The azimuthal and latitudinal grid lines are plotted every 15° in dotted line. The cross denotes the location of KSS.

subtropical jet around 30°S and the weak polar front jet around 50°S–60°S, consistent with the climatology of the jet flow variations explored by *Manney et al.* [2014].

In DJF (December, January, and February), the jet flow extends eastward from the east of South America to the south of Australia. The term ΔNBE indicates that significant imbalances at high latitudes occur in association with the jet flow, along with the midlatitude peaks over the continents. The strong imbalances associated with the jet flow are located (1) east of South America (45°S), (2) south of New Zealand (60°S), and (3) on the Southern Indian Ocean (60°S). In terms of *Ro*, there is additional potential imbalance region (4) northwest of the Andes (see Figure S2 in the supporting information). On the polar plane centered at the South Pole as shown in Figure 12, the region 1 is located about 2000 km northeast of KSS, and the regions 2 and 3 are located about 6000 km southwest and 6000 km southeast of KSS across the South Pole, respectively. In JJA (June, July, and August), there exists strong subtropical jet flow on the Southern Pacific Ocean and across Australia.

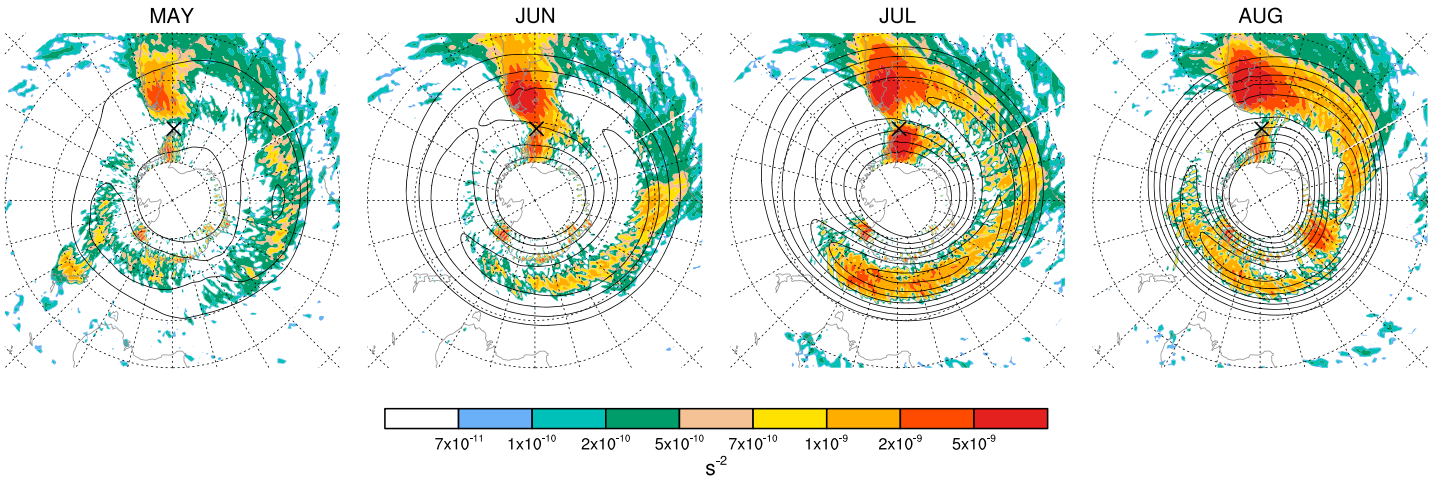

Figure 13. Same as Figure 12 but for May–August at 10 hPa. Contour lines of 40, 50, 60, 70, 80, 90, and 100 m s^{-1} for the wind magnitude are plotted.

Moderate imbalances related with the polar front jet are found (1) south of New Zealand (60°S) and (2) on the Southern Indian Ocean (60°S). Large imbalances are found (3) east of New Zealand on the Southern Pacific Ocean (30°S–45°S) in association with the strong subtropical jet flow.

Imbalances associated with the stratospheric jet flow can also generate IGWs that can be observed in the mesopause region over KSS. Several observational and numerical modeling studies have reported that the stratospheric jet flow (or polar night jet) is one of IGW sources over Antarctica by demonstrating downward energy propagation of IGWs in the lower stratosphere over the Antarctic areas [e.g., *Sato and Yoshiki*, 2008; *Yamashita et al.*, 2009; *Moffat-Griffin et al.*, 2011; *Sato et al.*, 2012; *Moffat-Griffin et al.*, 2013; *Murphy et al.*, 2014]. For the stratospheric jet (Figure 13) at 10 hPa ($z \approx 30$ km), the locations of the large imbalances are correlated with the jet exit regions in winter. On the polar plane, these imbalances may possibly generate the IGWs propagating in the W, NW, NE, or N direction over KSS since the imbalance regions are found over broad areas from northeast of KSS through southwest of KSS. However, it is notable that GWs observed over KSS do not exhibit strong NW propagation. Possible reasons may be revealed through ray tracing computation to be described below.

In order to ensure that GWs observed near the mesopause over KSS can be IGWs generated through the dynamical imbalances occurring around the jet flow systems, we perform global ray tracing model simulations. Global ray tracing formulations employed in this study are standard, in a sense that they are similar to those used in previous studies [e.g., *Marks and Eckermann*, 1995; *Song and Chun*, 2008; *Murphy et al.*, 2014]. The ray formulations are locally consistent with the IGW dispersion relation (4), but, on the larger scale, they include the spherical curvature effects formulated by *Hasha et al.* [2008] so that ray trajectories follow great circles in idealized situations where refraction due to the horizontal gradients of the atmospheric state variables is not present. For wave amplitude, the vertical flux of wave action ($c_{gz}A$, where A is the IGW action density defined as $E/\hat{\omega}$ and E is the IGW energy density) is assumed to be conserved following raypaths as in *Marks and Eckermann* [1995]. Wave saturation is computed using the vertical displacement (ζ_s) for saturated IGWs formulated by *Hasha et al.* [2008]. Critical-level filtering is computed through the saturation process since $\zeta_s \rightarrow 0$ as $\hat{\omega} \rightarrow |f|$ [see *Hasha et al.*, 2008, equation (18)]. Other dissipation mechanisms than the saturation process are not considered in this study.

For the time integration of the ray tracing equations, we employ a routine called DLSODA [*Petzold*, 1983], in the ODEPACK [*Hindmarsh*, 1983], that can automatically change algorithms depending on the degree of the stiffness in an ODE system. Interpolation of atmospheric state variables at ray positions is required to compute group velocities and wave number forcing terms, and it is achieved using a tricubic algorithm [*Lekien and Marsden*, 2005]. This tricubic scheme ensures the C^1 continuity and thus can produce spatially contiguous wave number forcing terms since the forcing terms are composed of the first-order spatial gradients of wind, stability, and density except for the curvature terms.

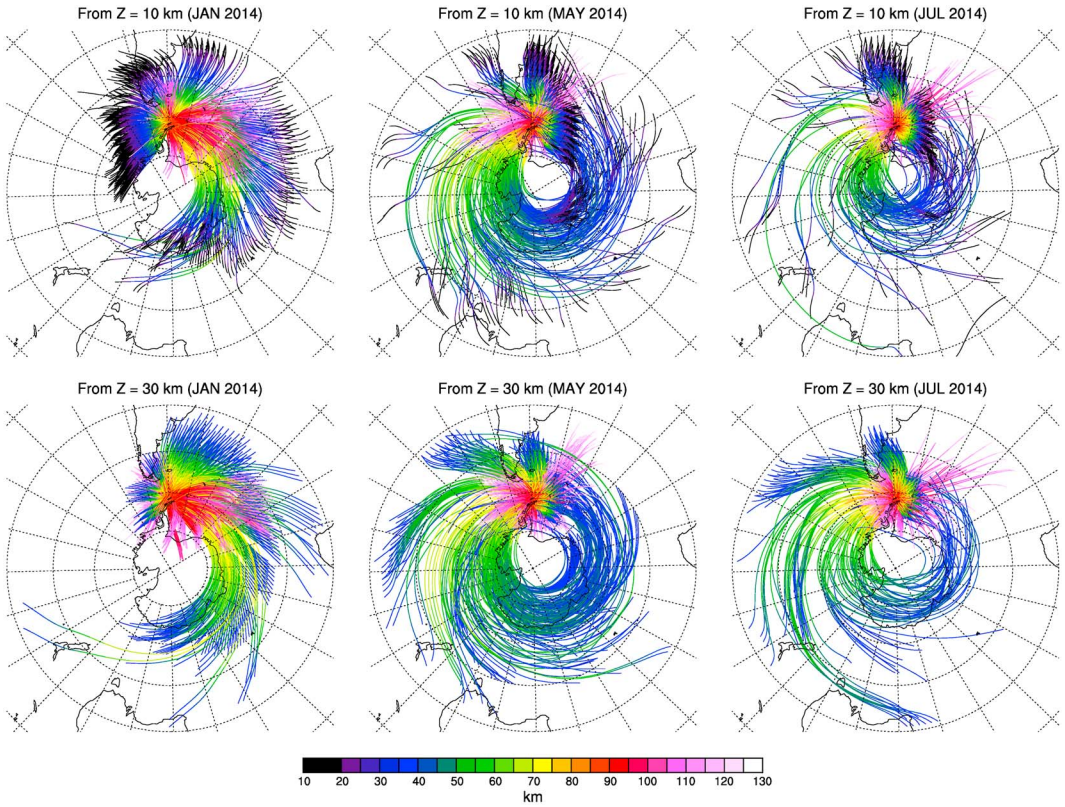

Figure 14. Trajectories of rays launched from (top row) z = 10 km and (bottom row) z = 30 km in January, May, and July. Rays that have the vertical wavelength of 15–30 km passing through the location of KSS at z = 85–95 km only are plotted. Ray trajectories are plotted in different colors depending on their heights.

Atmospheric wind, stability, and density data required for ray tracing simulations are obtained through the vertical fusion of the ERA data, the Modern-Era Retrospective Analysis for Research and Applications (MERRA) reanalysis [*Rienecker et al.*, 2011], NRLMSISE-00 empirical temperature model results [*Picone et al.*, 2002], and HWM14 [*Drob et al.*, 2015] and DWM07 [*Emmert et al.*, 2008] empirical horizontal wind model results. The NRLMSISE-00 model depends on the 10.7 cm solar flux and the 3-hourly geomagnetic indices (*Ap*). The HWM14 and DWM07 models require the *Ap* indices and are employed for geomagnetically quiet and disturbed times, respectively, but they do not depend on the solar flux. In the horizontal direction, the MERRA data are interpolated in the ERA grid, and the empirical models are computed in the same ERA grid. In the vertical direction, the ERA data, the MERRA data, and the empirical model results are acquired for the three overlapping pressure layers of 1000–1 hPa, 400–0.1 hPa, and $1-10^{-6}$ hPa, respectively. Then, vertically smooth curves represented by a linear combination of the third-order B-spline basis functions [*Piegl and Tiller*, 1997] are fit to the vertically overlapped atmospheric state variables. Wind and temperature obtained through the data fusion generally agree well with the reanalysis data such as the ERA and MERRA data and the empirical model results for 1000–0.1 hPa (z = 0–65 km) and $0.01-10^{-6}$ hPa ($z >$ 80 km), respectively (not shown in detail).

Ray tracing simulations are carried out for each atmospheric state at 00 UT, 06 UT, 12 UT, and 18 UT for seven selected days (1, 6, 11, 16, 21, 26, and 31) of January, May, and July. In total, 28 cases are simulated for each month. In each case, the atmospheric state variables are assumed not to change with time, and rays are launched at every other horizontal grid point between 30°S and 70°S at z = 10 and 30 km. Each simulation is run for 5 days. Initial rays are assumed to have the horizontal wavelength of 1000 km and the ground-based period of 4 h, which are consistent with the IGW properties analyzed in this study. The rays are initially assumed to propagate isotropically in the azimuthal direction at a 30° interval from each horizontal grid point. The vertical flux of wave action for the initial rays are determined such that the magnitudes of their pseudomomentum fluxes ($|\mathbf{k}|c_{gz}A$) can become 10^{-4} Pa. Satellite-estimated absolute values of spectrally integrated IGW pseudomomentum fluxes can amount to 10^{-2} Pa in the lower stratosphere ($z \approx 25$ km) over the southern

high-latitude regions (60°S–70°S) [e.g., *Ern et al.*, 2004, 2011]. Superpressure balloon observations [*Hertzog et al.*, 2008] indicate that the magnitude of the pseudomomentum flux can be $1-3\times10^{-3}$ Pa over the oceans between 50°S and 60°S. The magnitude of 10^{-4} Pa employed in this study is arbitrary, but it seems acceptable in a sense that IGWs employed in the ray tracing simulations are defined within a substantially narrow spectral range (i.e., IGWs with particular λ_h and ω) compared with broad spectra considered in the satellite and balloon observations.

Figure 14 demonstrates the trajectories of rays (launched from z = 10 and 30 km) that pass through the horizontal location of KSS (a latitude-longitude grid square with its side of 2° around the KSS location) and have the vertical wavelengths of 15–30 km (consistent with Figures 4 and 5) in the altitude range of 85–95 km where meteor echoes are most frequently found as shown in Figure 1. Trajectories of the rays generated at z = 10 km in January demonstrate that IGWs observed near the mesopause over KSS can be generated from the west of the Andes (30°S–45°S), from the Southern Atlantic Ocean east of South America (30°S–45°S), from the Southern Indian Ocean, or from the Southern Pacific Ocean (60°S–75°S) west of KSS. When compared with the ΔNBE at 200 hPa shown in Figure 12 (and *Ro* at 200 hPa in Figure S2), the west of the Andes and the Southern Atlantic Ocean are related to dynamical imbalances and thus can be possible source regions from which IGWs observed over KSS may be generated. These two regions are roughly located north of KSS. Therefore, IGWs generated from these regions may account for the N-S propagation (i.e., southward) revealed from the angular hodographs shown in Figure 11.

In May and July, comparison of Figure 14 with Figure 12 shows that the Southern Atlantic Ocean east of South America (30°S–45°S), the Southern Indian Ocean (30°S–45°S), and the south of Australia (45°S–60°S) can be potential source regions where IGWs can be generated. IGWs that emanated from the east of South America may propagate in the SW direction through mesopausal heights over KSS. IGWs generated in the other two regions (the Southern Indian Ocean and south of Australia) may be able to propagate long horizontal distance along the polar stratospheric jet axis and propagate in the NE direction near the mesopause over KSS. The SW direction after the short horizontal propagation and the NE direction after the long horizontal propagation may account for the NE-SW propagation in May and July, as revealed from the angular hodographs in Figure 11. As clearly seen in Figure 14, westward propagating IGWs generated in the Southern Indian Ocean are not found near the mesopause over KSS. This is because those IGWs may be Doppler shifted to the high intrinsic frequencies and they may already reach the mesopausal heights before they approach the location of KSS.

Figure 14 also shows that similar to the tropospheric jets, IGWs generated through dynamical imbalances at the stratospheric jet at z = 30 km can propagate in the NE direction over KSS in May and July. IGWs generated either from the south of Australia or from the Southern Indian Ocean can contribute to the observed IGWs propagating in the NE direction. These two regions correlate well with strong ΔNBE (or *Ro*) regions shown in Figure 13 (or Figure S3). Also, stratospheric IGWs generated from the east of South America are found to propagate in the SW direction near the mesopause over KSS as in the case of the tropospheric jets.

Mountains along the Andes can generate GWs that can be observed over KSS since the orographic GWs often spread leeward (southeastward) over the Southern Ocean east of South America, with their horizontal wave number vectors directed along the SW direction [*Wu and Eckermann*, 2008; *Alexander and Teitelbaum*, 2011; *Sato et al.*, 2012]. As shown in Figure 12, the term ΔNBE at 200 hPa is strong over rough topography as well as around the strong jet regions over the ocean, since rough topography can induce strong horizontal divergence, and the term ΔNBE is actually the forcing term of the horizontal divergence equation. However, mountain waves around the Andes are usually quasi-stationary and often found to have small horizontal wavelengths of about 100–300 km [e.g., *Alexander and Teitelbaum*, 2011]. Therefore, in spite of potential importance of mountain waves, these waves may not appear in the analysis of this study since we employ meteor radar wind averaged over the areas with the radius of 250–300 km and consider only traveling GWs with ground-based periods smaller than 4.5 h.

Large-scale convective systems such as typhoons can also be candidates for the sources of IGWs observed over KSS. As *Liu et al.* [2014] demonstrated, tropical cyclones located at 20°S can induce GWs that can propagate southward up to the coastlines of Antarctica at the altitude of the mesopause. In the Southern Hemisphere, tropical storms are occasionally generated over the Pacific Ocean north of New Zealand and are fairly rare over the Atlantic Ocean [*Mendelsohn et al.*, 2012]. IGWs associated with tropical storms may be observed in

the mesopause region over KSS, but they seem to be much less frequently observed compared with IGWs induced from the vigorous and ever-present tropospheric jets over the Southern Ocean and from the strong stratospheric jet flow.

5. Summary and Conclusion

Wind observations have been made using a meteor radar at King Sejong Station (62.22°S, 58.78°W) north of the Antarctic Peninsula since 2007, and the data for the whole year of 2014 are employed to understand characteristics of IGWs and their seasonal variations in the southern polar mesopause region. Observed horizontal wind components are temporally and vertically binned at the regular intervals of 2 min and 3 km, respectively.

The LS spectral analysis is carried out for overlapped 5 day time series (stepped by 1 day) to isolate IGWs from the large-scale flow, considering irregularly distributed missing data. Band-pass filtering of the spectral analysis results allows for the separation of the large-scale flow and GW signals in the observed wind. For band-pass filtering, the cutoff periods of 4.5 h and 5.5 h are employed assuming that IGWs have ground-based periods of less than 4.5 h, and the large-scale flow has ground-based period of larger than 5.5 h such that it can include the constant mean wind, four major tidal waves (24 h, 12 h, 8 h, and 6 h) and planetary waves. The simulation for specified tidal and IGW motions demonstrates that the LS spectral analysis and band-pass filtering are capable of properly separating GW signals and large-scale flow from the observed meteor radar wind.

In the IGW signals separated from the observed winds, it is found that vertically propagating low-frequency IGWs are frequently detected (in about 34% of the 1 year time period) in the mesopause region over KSS. Downward phase progression of IGW horizontal wind components and their counterclockwise rotation in time are frequently found throughout the year 2014. These results suggest that most of the detected IGWs transport their energy upward, implying that their sources should mainly be located below the mesopause region. Hodograph analysis based on the Stokes parameter method shows that most of GWs are low-frequency IGWs with intrinsic frequencies of $|f| - 3|f|$. Such IGWs seem to have fairly large vertical wavelengths of 14–28 km, consistent with other relevant studies on IGWs in the southern polar mesopause region. The dispersion relation suggests that these IGWs may have horizontal wavelengths of 400–1000 km for intrinsic frequencies of $2|f| - 3|f|$ and 700–3000 km for intrinsic frequencies of $|f| - 2|f|$. When background wind variations are not considered, these IGWs with intrinsic frequencies of $2|f| - 3|f|(|f| - 2|f|)$ can have horizontal and vertical components of group velocity of 5500 km d^{-1} and 160 km d^{-1} (3200 km d^{-1} and 32 km d^{-1}), respectively.

Hodograph analysis also provides information of the horizontal propagation direction of IGWs, albeit with 180° ambiguity. The horizontal propagation direction clearly exhibits seasonal variations. In DJF, the N-S propagation is predominant, while in JJA, the NE-SW propagation is more pronounced. These propagation directions seem to be consistent with the horizontal distributions of strong nonlinear imbalances associated with the tropospheric subtropic and polar jet-front systems. Seasonal variation of the tropospheric jet flow shows that two separate (subtropical and polar front) jet flow systems appear around the South Pole in JJA, but the two jet flow systems are merged in DJF. As revealed from downward energy propagation in the lower stratosphere in previous studies, midstratospheric polar night jet may also be one of sources of the observed IGWs in the mesopause region, especially in May–August.

Ray tracing results indicate that the N-S propagation in summer may be due to the jet flow systems either roughly north of KSS or over the Southern Atlantic Ocean, and the NE-SW propagation in winter may be either the SW propagation from the jet flow systems northeast of KSS or the NE propagation (around the South Pole) from the south of Australia and Southern Indian Ocean. Westward propagating IGWs generated in the troposphere from the Southern Indian Ocean may not be observed in the mesopause over KSS due to the Doppler shifting to high intrinsic frequencies (large vertical wavelengths) by the strong stratospheric eastward jet. The stratospheric sources located south of Australia or over the Southern Indian Ocean (east of South America) can also be responsible for the NE (SW) propagation of the observed IGWs over KSS in winter. Large-scale convective systems such as tropical cyclones may also be sources for IGWs observed over KSS, but their influences may be limited since they are much less frequently generated in the Southern Hemisphere compared with the ever-present jet flow systems over the Southern Ocean. Mountains along the Andes are not considered for possible forcing mechanisms in this study since quasi-stationary GWs with small horizontal wavelengths are excluded in the initial wind processing and bandpass filtering procedures.

Acknowledgments
This work was supported by research fund PE17020 from Korea Polar Research Institute. ERA-Interim data are available through http://apps.ecmwf.int. MERRA products are available through http://disc.sci.gsfc.nasa.gov/daac-bin/DataHoldings.pl. HWM14 is available as a part of the supporting information of *Drob et al.* [2015] at http://onlinelibrary.wiley.com/doi/10.1002/2014EA0000089. DWM07 and NRLMSISE-00 are available through http://ccmc.gsfc.nasa.gov/modelweb. Geomagnetic (*Ap*) and solar activity ($F_{10.7}$) indices are downloaded at ftp://ftp.ngdc.noaa.gov/STP/GEOMAGNETIC_DATA/INDICES/KP_AP. Meteor radar observational data employed in this study and IGW analysis results are available upon request (isong@kopri.re.kr). The authors would like to express their appreciation for the valuable comments by reviewers. The comments significantly improved the original manuscript.

References

Akmaev, R. A., J. M. Forbes, F.-J. Lübken, D. J. Murphy, and J. Höffner (2015), Tides in the mesopause region over Antarctica: Comparison of whole atmosphere model simulations with ground-based observations, *J. Geophys. Res. Atmos*, *121*, 1156–1169, doi:10.1002/2015JD023673.

Alexander, M. J., and H. Teitelbaum (2011), Three-dimensional properties of Andes mountain waves observed by satellite: A case study, *J. Geophys. Res.*, *116*, D23110, doi:10.1029/2011JD016151.

Andrews, D. G., J. R. Holton, and C. B. Leovy (1987), *Middle Atmosphere Dynamics*, Academic, Orlando, Fla.

Beldon, C. L., and N. J. Mitchell (2010), Gravity wave-tidal interactions in the mesosphere and lower thermosphere over Rothera, Antarctica (68°S, 68°W), *J. Geophys. Res.*, *115*, D18101, doi:10.1029/2009JD013617.

Born, M., and E. Wolf (1999), *Principles of Optics: Electromagnetic Theory of Propagation, Interference and Diffraction of Light*, Cambridge Univ., New York.

Chandran, A., D. W. Rusch, S. E. Palo, G. E. Thomas, and M. J. Taylor (2009), Gravity wave observations in the summertime polar mesosphere from the Cloud Imaging and Particle Size (CIPS) experiment on the AIM spacecraft, *J. Atmos. Sol. Terr. Phys.*, *71*, 392–400, doi:10.1016/j.jastp.2008.09.041.

Chen, C., X. Chu, A. J. McDonald, S. L. Vadas, Z. Yu, W. Fong, and X. Lu (2013), Inertia-gravity waves in Antarctica: A case study using simultaneous lidar and radar measurements at McMurdo/Scott Base (77.8°S, 166.7°E), *J. Geophys. Res. Atmos.*, *118*, 2794–2808, doi:10.1002/jgrd.50318.

Chen, C., X. Chu, J. Zhao, B. R. Roberts, Z. Yu, W. Fong, X. Lu, and J. A. Smith (2016), Lidar observations of persistent gravity waves with periods of 3–10 h in the Antartic middle and upper atmosphere at McMurdo (77.83°S, 166.67°E), *J. Geophys. Res. Space Physics*, *121*, 1483–1502, doi:10.1002/2015JA022127.

Chun, H.-Y., I.-S. Song, and J.-J. Baik (2006), Seasonal variations of gravity waves revealed in rawinsonde data at Pohang, Korea, *Meteorol. Atmos. Phys.*, *93*, 255–273, doi:10.1007/s00703-005-0164-5.

Dee, D. P., et al. (2011), The ERA-Interim reanalysis: Configuration and performance of the data assimilation system, *Q. J. R. Meteorol. Soc.*, *137*, 553–597, doi:10.1002/qj.828.

de Wit, R. J., R. E. Hibbins, P. J. Espy, Y. J. Orsolini, V. Limpasuvan, and D. E. Kinnison (2014), Observations of gravity wave forcing of the mesopause region during the January 2013 major Sudden Stratospheric Warming, *Geophys. Res. Lett.*, *41*, 4745–4752, doi:10.1002/2014GL060501.

Drob, D. P., et al. (2015), An update to the horizontal wind model (HWM): The quiet time thermosphere, *Earth Space Sci.*, *2*, 301–319, doi:10.1002/2014EA000089.

Du, J., and W. E. Ward (2010), Terdiurnal tide in the extended Canadian Middle Atmospheric Model (CMAM), *J. Geophys. Res.*, *115*, D24106, doi:10.1029/2010JD014479.

Eckermann, S. D. (1996), Hodographic analysis of gravity waves: Relationships among Stokes parameters, rotary spectra and cross-spectral methods, *J. Geophys. Res.*, *101*, 19169–19174, doi:10.1029/96JD01578.

Emmert, J. T., D. P. Drob, G. G. Shepherd, G. Hernandez, M. J. Jarvis, J. W. Meriwether, R. J. Niciejewski, D. P. Sipler, and C. A. Tepley (2008), DWM07 global empirical model of upper thermospheric storm-induced disturbance winds, *J. Geophys. Res.*, *113*, A11319, doi:10.1029/2008JA013541.

Ern, M., P. Preusse, M. J. Alexander, and C. D. Warner (2004), Absolute values of gravity wave momentum flux derived from satellite data, *J. Geophys. Res.*, *109*, D20103, doi:10.1029/2004JD004752.

Ern, M., P. Preusse, J. C. Gille, C. L. Hepplewhite, M. G. Mlynzczak, J. M. Russell III, and M. Riese (2011), Implications for atmospheric dynamics derived from global observations of gravity wave momentum flux in stratosphere and mesosphere, *J. Geophys. Res.*, *116*, D19107, doi:10.1029/2011JD015821.

Fritts, D. C., and M. J. Alexander (2003), Gravity wave dynamics and effects in the middle atmosphere, *Rev. Geophys.*, *41*(1), 1003, doi:10.1029/2001RG000106.

Fritts, D. C., and R. A. Vincent (1987), Mesospheric momentum flux studies at Adelaide, Australia: Observations and a gravity wave-tidal interaction model, *J. Atmos. Sci.*, *44*, 605–619, doi:10.1175/1520-0469(1987)044<0605:MMFSAA>2.0.CO;2.

Fritts, D. C., J. R. Isler, G. E. Thomas, and Ø. Andreassen (1993), Wave breaking signatures in noctilucent clouds, *Geophys. Res. Lett.*, *20*, 2039–2042, doi:10.1029/93GL01982.

Fritts, D. C., et al. (2010a), Southern Argentina Agile Meteor Radar: System design and initial measurements of large-scale winds and tides, *J. Geophys. Res.*, *115*, D18112, doi:10.1029/2010JD013850.

Fritts, D. C., D. Janches, and W. K. Hocking (2010b), Southern Argentina Agile Meteor Radar: Initial assessment of gravity wave momentum fluxes, *J. Geophys. Res.*, *115*, D19123, doi:10.1029/2010JD013891.

Hasha, A., O. Bühler, and J. Scinocca (2008), Gravity wave refraction by three-dimensionally varying winds and the global transport of angular momentum, *J. Atmos. Sci.*, *65*, 2892–2906, doi:10.1175/2007JAS2561.1.

Hertzog, A., G. Boccara, R. A. Vincent, F. Vial, and P. Cocquerez (2008), Estimation of gravity wave momentum flux and phase speeds from quasi-Lagrangian stratospheric balloon flights. Part II: Results from the Vorcore campaign in Antarctica, *J. Atmos. Sci.*, *65*, 3056–3070, doi:10.1175/2008JAS2709.1.

Hindmarsh, A. C. (1983), ODEPACK, a systematized collection of ODE solvers, in *Scientific Computing*, edited by R. S. Stepleman et al., pp. 55–64, North-Holland, Amsterdam.

Hines, C. O. (1989), Tropopausal mountain waves over Arecibo: A case study, *J. Atmos. Sci.*, *46*, 476–488, doi:10.1175/1520-0469(1989)046<0476:TMWOAA>2.0.CO;2.

Hocke, K., and N. Kämpfer (2009), Gap filling and noise reduction of unevenly sampled data by means of the Lomb-Scargle periodogram, *Atmos. Chem. Phys.*, *9*, 4197–4206, doi:10.5194/acp-9-4197-2009.

Hocking, W. K. (2005), A new approach to momentum flux determinations using SKiYMET meteor radars, *Ann. Geophys.*, *23*, 2433–2439, doi:10.5194/angeo-23-2433-2005.

Hocking, W. K., and T. Thayaparan (1997), Simultaneous and colocated observation of winds and tides by MF and meteor radars over London, Canada (43°N, 81°W), during 1994–1996, *Radio Sci.*, *32*, 833–865, doi:10.1029/96RS03467.

Jee, G., J.-H. Kim, C. Lee, and Y. H. Kim (2014), Ground-based observations for the upper atmosphere at King Sejong Station, Antarctica, *J. Astron. Space Sci.*, *31*, 169–176, doi:10.5140/JASS.2014.31.2.169.

Kam, H., Y. Kim, G. Jee, Y.-B. Ham, and I.-S. Song (2016), Analysis of propagating characteristics of mesospheric short period gravity waves observed at the Antarctic Peninsula, paper presented at 3rd International Antarctic Gravity Wave Instrument Network (ANGWIN) Science Workshop, Cambridge, U. K., 12–14 Apr.

Kim, J.-H., Y. H. Kim, G. Jee, and C. Lee (2012), Mesospheric temperature estimation from meteor decay times of weak and strong meteor trails, *J. Atmos. Sol. Terr. Phys.*, *89*, 18–26, doi:10.1016/j.jastp.2012.07.003.

Kim, Y.-J., S. D. Eckermann, and H.-Y. Chun (2003), An overview of the past, present and future of gravity-wave drag parameterization for numerical climate and weather prediction models, *Atmos. Ocean*, *41*, 65–98, doi:10.3137/ao.410105.
Kim, Y. H., J. K. Chung, and Y. I. Won (2004), Observation of a persistent Leonid meteor train with an all-sky camera, *J. Atmos. Terr. Phys.*, *66*, 1001–1009, doi:10.1016/j.jastp.2004.03.007.
Kim, Y. H., C. Lee, J.-K. Chung, J.-H. Kim, and H.-Y. Chun (2010), Seasonal variations of mesospheric gravity waves observed with an airglow all-sky camera at Mt. Bohyun, Korea (36°N), *J. Astron. Space Sci.*, *27*, 181–188, doi:10.5140/JASS.2010.27.3.181.
Lee, C., Y. H. Kim, J.-H. Kim, G. Jee, Y.-I. Won, and D. L. Wu (2013), Seasonal variation of wave activities near the mesopause region observed at King Sejong Station (62.22°S, 58.78°W), Antarctica, *J. Atmos. Sol. Terr. Phys.*, *105-106*, 30–38, doi:10.1016/j.jastp.2013.07.006.
Lekien, F., and J. Marsden (2005), Tricubic interpolation in three dimension, *Int. J. Numer. Meth. Engng.*, *63*, 455–471, doi:10.1002/nme.1296.
Lindzen, R. S. (1981), Turbulence and stress due to gravity wave and tidal breakdown, *J. Geophys. Res.*, *86*, 9707–9714, doi:10.1029/JC086iC10p09707.
Liu, H.-L., J. M. McInerney, S. Santos, P. H. Lauritzen, M. A. Taylor, and N. M. Pendatella (2014), Gravity waves simulated by high-resolution Whole Atmosphere Community Climate Model, *Geophys. Res. Lett.*, *41*, 9106–9112, doi:10.1002/2014GL062468.
Lomb, N. R. (1976), Least-squares frequency analysis of unequally spaced data, *Adv. Space Sci.*, *39*, 447–462, doi:10.1007/BF00648343.
Marks, C. J., and S. D. Eckermann (1995), A three-dimensional nonhydrostatic ray-tracing model for gravity waves: Formulation and preliminary results for the middle atmosphere, *J. Atmos. Sci.*, *52*, 1959–1984, doi:10.1175/1520-0469(1995)052<1959:ATDNRT>2.0.CO;2.
Manney, G. L., M. I. Hegglin, W. H. Daffer, M. J. Schwartz, M. L. Santee, and S. Pawson (2014), Climatology of Upper Tropospheric-Lower Stratospheric (UTLS) jets and tropopauses in MERRA, *J. Clim.*, *27*, 3248–3271, doi:10.1175/JCLI-D-13-00243.1.
Mendelsohn, R., K. Emanuel, S. Chonabayahi, and L. Bakkensen (2012), The impact of climate change on global tropical cyclone damage, *Nat. Clim. Change*, *2*, 205–209, doi:10.1038/nclimate1357.
Mitchell, N. J., D. Pancheva, H. R. Middleton, and M. E. Hagan (2002), Mean winds and tides in the Arctic mesosphere and lower thermosphere, *J. Geophys. Res.*, *107*(A1), 1004, doi:10.1029/2001JA900127.
Moffat-Griffin, T., R. E. Hibbins, M. J. Jarvis, and S. R. Colwell (2011), Seasonal variations of gravity wave activity in the lower stratosphere over an Antarctic Peninsula station, *J. Geophys. Res.*, *116*, D14111, doi:10.1029/2010JD015349.
Moffat-Griffin, T., M. J. Jarvis, S. R. Colwell, A. J. Kavanagh, G. L. Manney, and W. H. Daffer (2013), Seasonal variations in lower stratospheric gravity wave energy above the Falkland Islands, *J. Geophys. Res. Atmos.*, *118*, 10,861–10,869, doi:10.1002/jgrd.50859.
Murphy, D. J., M. Tsutsumi, D. M. Riggin, G. O. L. Jones, R. A. Vincent, M. E. Hagan, and S. K. Avery (2003), Observations of a nonmigrating component of the semidiurnal tide over Antarctica, *J. Geophys. Res.*, *108*(D8), 4241, doi:10.1029/2002JD003077.
Murphy, D. J., et al. (2006), A climatology of tides in the Antarctic mesosphere and lower thermosphere, *J. Geophys. Res.*, *111*, D23104, doi:10.1029/2005JD006803.
Murphy, D. J., S. P. Alexander, A. R. Klekociuk, P. T. Love, and R. A. Vincent (2014), Radiosonde observations of gravity waves in the lower stratosphere over Davis, Antarctica, *J. Geophys. Res. Atmos.*, *119*, 11,973–11,996, doi:10.1002/2014JD022448.
Nastrom, G. D., and D. C. Fritts (1992), Sources of mesoscale variability of gravity waves. Part I: Topographic excitation, *J. Atmos. Sci.*, *49*, 101–110, doi:10.1175/1520-0469(1992)049<0101:SOMVOG>2.0.CO;2.
Nicolls, M. J., R. H. Varney, S. L. Vadas, P. A. Stamus, C. J. Heinselman, R. B. Cosgrove, and M. C. Kelley (2010), Influence of an inertia-gravity wave on mesospheric dynamics: A case study with the Poker Flat Incoherent Scatter Radar, *J. Geophys. Res.*, *115*, D00N02, doi:10.1029/2010JD014042.
Nielsen, K., M. J. Taylor, R. E. Hibbins, and M. J. Jarvis (2009), Climatology of short-period mesospheric gravity waves over Halley, Antarctica (76°S, 27°W), *J. Atmos. Sol. Terr. Phys.*, *71*, 991–1000, doi:10.1016/j.jastp.2009.04.005.
O'Sullivan, D. J., and T. J. Dunkerton (1995), Generation of inertia-gravity waves in a simulated life cycle of baroclinic instability, *J. Atmos. Sci.*, *52*, 3695–3716, doi:10.1175/1520-0469(1995)052<3695:GOIWIA>2.0.CO;2.
Oyama, S., and B. J. Watkins (2012), Generation of atmospheric gravity waves in the polar thermosphere in response to auroral activity, *Space Sci. Rev.*, *168*, 463–473, doi:10.1007/s11214-011-9847-z.
Pautet, P.-D., J. Stegman, C. M. Wrasse, K. Nielsen, H. Takahashi, M. J. Taylor, K. W. Hoppel, and S. D. Eckermann (2011), Analysis of gravity waves structures visible in noctilucent cloud images, *J. Atmos. Sol. Terr. Phys.*, *73*, 2082–2090, doi:10.1016/j.jastp.2010.06.001.
Petzold, L. (1983), Automatic selection of methods for solving stiff and nonstiff systems of ordinary differential equations, *SIAM J. Sci. Stat. Comput.*, *4*, 136–148, doi:10.1137/0904010.
Picone, J. M., A. E. Hedin, D. P. Drob, and A. C. Aikin (2002), NRLMSISE-00 empirical model of the atmosphere: Statistical comparisons and scientific issues, *J. Geophys. Res.*, *107*(A12), 1468, doi:10.1029/2002JA009430.
Piegl, L., and W. Tiller (1997), *The NURBS Book*, 646 pp., Springer, Berlin.
Plougonven, R., and F. Zhang (2014), Internal gravity waves from atmospheric jets and fronts, *Rev. Geophys.*, *52*, 33–76, doi:10.1002/2012RG000419.
Plougonven, R., H. Teitelbaum, and V. Zeitlin (2003), Inertia-gravity wave generation by the tropospheric mid-latitude jet as given by the FASTEX radiosoundings, *J. Geophys. Res.*, *108*(D21), 4686, doi:10.1029/2003JD003535.
Press, W. H., S. A. Teukolsky, W. T. Vetterling, and B. P. Flannery (1992), *Numerical Recipes in Fortran: The Art of Scientific Computing*, Cambridge Univ., New York.
Qian, L., S. C. Solomon, and T. J. Kane (2009), Seasonal variation of thermosphereic density and composition, *J. Geophys. Res.*, *114*, A01312, doi:10.1029/2008JA013643.
Reid, I. M., and R. A. Vincent (1987a), Measurements of mesospheric gravity wave momentum fluxes and mean flow accelerations at Adelaide, Australia, *J. Atmos. Terr. Phys.*, *49*, 443–460, doi:10.1016/0021-9169(87)90039-0.
Reid, I. M., and R. A. Vincent (1987b), Measurements of the horizontal scales and phase velocities of short period mesospheric gravity waves at Adelaide, Australia, *J. Atmos. Terr. Phys.*, *49*, 1033–1048, doi:10.1016/0021-9169(87)90110-3.
Rienecker, M. M., et al. (2011), MERRA: NASA's Modern-Era Retrospective Analysis for Research and Applications, *J. Clim.*, *24*, 3624–3648, doi:10.1175/JCLI-D-11-00015.1.
Sato, K. (1993), Small-scale wind disturbances observed by the MU radar during the passage of typhoon Kelly, *J. Atmos. Sci.*, *50*, 518–537, doi:10.1175/1520-0469(1993)050<0518:SSWDOB>2.0.CO;2.
Sato, K., and M. Yoshiki (2008), Gravity wave generation around the polar vortex in the stratosphere revealed by 3-hourly radiosonde observations at Syowa station, *J. Atmos. Sci.*, *65*, 3719–3735, doi:10.1175/2008JAS2539.1.
Sato, K., S. Tateno, S. Watanabe, and Y. Kawatani (2012), Gravity wave characteristics in the Southern Hemisphere revealed by a high-resolution middle-atmosphere general circulation model, *J. Atmos. Sci.*, *69*, 1378–1396, doi:10.1175/JAS-D-11-0101.1.
Scargle, J. D. (1982), Studies in astronomical time series analysis. II. Statistical aspects of spectral analysis of unevenly spaced data, *Astrophys. J.*, *263*, 835–853, doi:10.1086/160554.
Smith, A. K. (2012), Global dynamics of the MLT, *Surv. Geophys.*, *33*, 1177–1230, doi:10.1007/s10712-012-9196-9.

Smith, A. K., D. V. Pancheva, and N. J. Mitchell (2004), Observations and modeling of the 6-hour tide in the upper mesosphere, *J. Geophys. Res.*, *109*, D10105, doi:10.1029/2003JD004421.

Song, I.-S., and H.-Y. Chun (2008), A Lagrangian spectral parameterization of gravity wave drag induced by cumulus convection, *J. Atmos. Sci.*, *65*, 1204–1224, doi:10.1175/2007JAS2369.1.

Suzuki, S., S. L. Vadas, K. Shiokawa, Y. Otsuka, S. Kawamura, and Y. Murayama (2013a), Typhoon-induced concentric airglow structures in the mesopause region, *Geophys. Res. Lett.*, *40*, 5983–5987, doi:10.1002/2013GL058087.

Suzuki, H., T. Nakamura, S. L. Vadas, M. Tsutsumi, and M. Taguchi (2013b), Inertia-gravity wave in the polar mesopause region inferred from successive images of a meteor train, *J. Geophys. Res. Atmos.*, *118*, 3047–3052, doi:10.1002/jgrd.50228.

Taylor, M. J., and M. A. Hapgood (1990), On the origin of ripple-type wave structure in the OH nightglow emission, *Planet. Space Sci.*, *38*, 1421–1430, doi:10.1016/0032-0633(90)90117-9.

Thorsen, D., S. J. Franke, and E. Kudeki (1997), A new approach to MF radar interferometry for estimating mean winds and momentum flux, *Radio Sci.*, *32*, 707–726, doi:10.1029/96RS03422.

Uccelini, L., and S. Koch (1987), The synoptic setting and possible energy sources for mesoscale wave disturbances, *Mon. Weather Rev.*, *115*, 721–729, doi:10.1175/1520-0493(1987)115<0721:TSSAPE>2.0.CO;2.

Vadas, S. L., and H.-L. Liu (2013), Numerical modeling of the large-scale neutral and plasma responses to the body forces created by the dissipation of gravity waves from 6 h of deep convection in Brazil, *J. Geophys. Res. Space Physics*, *118*, 2593–2617, doi:10.1002/jgra.50249.

Vincent, R. A., and S. D. Eckermann (1990), VHF radar observations of mesoscale motions in the troposphere: Evidence for gravity wave Doppler shifting, *Radio Sci.*, *25*, 1019–1037, doi:10.1029/RS025i005p01019.

Vincent, R. A., and D. C. Fritts (1987), A climatology of gravity wave motions in the mesopause region at Adelaide, Australia, *J. Atmos. Sci.*, *44*, 748–760, doi:10.1175/1520-0469(1987)044<0748:ACOGWM>2.0.CO;2.

Wang, L., M. A. Geller, and M. J. Alexander (2005), Spatial and temporal variations of gravity wave parameters. Part I: Intrinsic frequency, wavelength, and vertical propagation direction, *J. Atmos. Sci.*, *62*, 125–142, doi:10.1175/JAS-3364.1.

Wu, D. L., and S. D. Eckermann (2008), Global gravity wave variances from Aura MLS: Characteristics and interpretation, *J. Atmos. Sci.*, *65*, 3695–3718, doi:10.1175/2008JAS2389.1.

Yamashita, C., X. Chu, H.-L. Liu, P. J. Espy, G. J. Nott, and W. Huang (2009), Stratospheric gravity wave characteristics and seasonal variations observed by lidar at the South Pole and Rothera, Antarctica, *J. Geophys. Res.*, *114*, D12101, doi:10.1029/2008JD011472.

Yiğit, E., A. S. Medvedev, S. L. England, and T. J. Immel (2013), Simulated variability of the high-latitude thermosphere induced by small-scale gravity waves during a sudden stratospheric warming, *J. Geophys. Res. Space Physics*, *119*, 357–365, doi:10.1002/2013JA019283.

Zhang, F. (2004), Generation of mesoscale gravity waves in the upper-tropospheric jet-front systems, *J. Atmos. Sci.*, *61*, 440–457, doi:10.1175/1520-0469(2004)061<0440:GOMGWI>2.0.CO;2.

Zhang, F., C. A. Davis, M. L. Kaplan, and S. E. Koch (2001), Wavelet analysis and the governing dynamics of a large-amplitude mesoscale gravity-wave event along the East Coast of the United States, *Q. J. R. Meteorol. Soc.*, *127*, 2209–2245, doi:10.1002/qj.49712757702.